Constitutive modelling of glassy polymers considering shear plasticity and craze yielding

Zhouzhou Pan[a], Huanming Chen[a], Laurence Brassart[a,*]

[a]*Department of Engineering Science, University of Oxford, Oxford OX1 3PJ, United Kingdom*

Abstract

The inelastic behaviour of thermoplastic polymers below the glass transition temperature can involve shear plasticity or crazing, depending on the strain rate and temperature. Shear plasticity is driven by local shear stresses and is essentially volume preserving. In contrast, crazing is a failure phenomenon occurring under tension and causes significant volume change. In some cases, crazing can also result in large inelastic deformations at macroscopic scale, referred to as craze yielding. The aim of this study is to propose a thermodynamically-consistent constitutive framework that accounts for both shear plasticity and craze yielding in glassy polymers. The main assumption is that shear plasticity and craze yielding occur exclusively from each other, depending on the local stress state. Both are modelled as thermally-activated processes with different activation stresses and flow rules. The theory is validated against experimental data for polylactic acid (PLA). Our model is capable of reproducing the stress-strain response including yielding, softening, and drawing under both shear plasticity and craze yielding, and also accurately predicts the volumetric deformation under tension. In particular, our simulations well capture the interesting phenomenon that craze yielding stabilises localised deformations and prevents necking. Our model can also simulate complex scenarios where both mechanisms occur simultaneously at different locations of the specimen.

Keywords: Crazing; Dilatational plasticity; Thermally activated process; Amorphous polymer; PLA; Large deformations

*Corresponding author.
Email address: laurence.brassart@eng.ox.ac.uk (Laurence Brassart)

1. Introduction

Depending on the strain rate and temperature, thermoplastic polymers below their glass transition temperature can exhibit two distinct forms of inelastic response under loading, namely shear yielding and crazing (Argon, 2013; Deblieck et al., 2011). Shear yielding is a distortional plasticity deformation mode resulting from localised structural rearrangements ("shear transformation zones") in response to local shear stresses. Under shear yielding dominated deformation, a polymer is capable of undergoing significantly large inelastic deformations, typically involving yielding, post-yield softening and rehardening. In contrast, crazing refers to a failure mechanism involving the formation of microvoids (crazes) whose surfaces are bridged by many fine fibrils aligned with the maximum principal tensile stress. The polymer chains surrounding these crazes are constantly drawn into the craze fibrils, causing craze propagation. As the crazes propagate and expand, the fibril structures eventually break down, leading to the formation of macroscopic cracks and final failure (Deblieck et al., 2011). Although crazing often leads to brittle fracture prior to the yield point, crazing can also result in large, dilatational plastic deformations at macroscopic scale before failure, as seen for example in some glassy polymers and rubber-toughened polymers (Hoare and Hull, 1972; Narisawa, 1972; G'sell et al., 2002; Van der Giessen and Seelig, 2015; McCutcheon et al., 2020; Razavi et al., 2020). Stress-strain curves then exhibit features similar to shear yielding, including yielding followed by softening, steady flow, and even hardening. In this work, we refer to the dilatational plastic deformation mediated by crazing as "craze yielding".

Over the last few decades, considerable efforts have been dedicated to developing constitutive models for predicting the large viscoplastic deformations of glassy polymers during shear yielding. Haward and Thackray (1968) pioneered the field in recognising that the material must overcome two distinct sources of resistance when subjected to large viscoplastic deformations, i.e. a rate and temperature dependent intermolecular resistance and a configurational entropy resistance due to the alignment of entangled polymer chains. Based on this concept, they proposed a one-dimensional rheological model by connecting a Hookean spring in series with an Eyring dashpot and Langevin spring in parallel. Following their work, the framework was extensively refined and extended to describe the mechanical response of thermoplastic polymers under complex loading over a wide range of strain rates and temperatures, mainly through modification of the thermally-

activated flow rule to refine the description of the flow mechanism (Boyce et al., 1988; Buckley and Jones, 1995; Hasan and Boyce, 1995; Bergström and Boyce, 1998; Govaert et al., 2000; Anand et al., 2009; Xiao et al., 2022; Lin et al., 2023), by using advanced rubber elasticity models for describing the hardening due to molecular alignment (Arruda and Boyce, 1993; Wu and Van Der Giessen, 1993; Tervoort and Govaert, 2000; Wang et al., 2021), or by introducing additional viscoplastic branches or elements (Mulliken and Boyce, 2006; Alves et al., 2023; Liu et al., 2022).

Regarding the modelling of crazing, early studies mainly focused on establishing criteria for craze initiation and on unravelling the mechanisms for craze growth. Based on a series of experimental observations for PMMA, Sternstein and Ongchin (1969) proposed that crazes initiate when the stress bias (defined as the absolute value of the difference between the first and second principal Cauchy stresses in plane stress) equals a critical value that depends on the mean normal stress. Although the stress-bias criterion provides good fitting in some cases, it lacks a mechanistic foundation, since the stress bias is in fact a measure of shear stress, while crazes initiate and grow in the direction of maximum principal tensile stress (Bucknall, 2007a; Argon, 2011). Furthermore, the stress-bias criterion is limited to plane stress and is not applicable in the case where the two largest principal stresses are close to each other, since the stress bias approaches zero. Later, Oxborough and Bowden (1973) developed a critical-strain criterion in which crazing initiates when the maximum principal strain reaches a critical value, which is in better agreement with the mechanism of crazing onset but still suffers from the difficulty in application, since it requires knowledge of the local strain state near the initiation site of individual crazes (Oxborough and Bowden, 1973). Inspired by descriptions of ductile fracture in metals, Argon (1973b) proposed a micromechanical model by assuming that the nucleation of individual nanovoids follows Arrhenius' equation under deviatoric shear stress in the regions of high stress concentration and are subsequently expanded by the mean normal stress. Realising that this model was not applicable to craze propagation, Argon and Hannoosh (1977) proposed the interface evolution mechanism for craze growth known as the meniscus instability concept. Based on this concept, Kramer (1983) derived a stress-based craze propagation criterion depending on the surface energy associated with the formation of crazes, yield stress and strain rate.

Recent studies have incorporated the fundamental understanding of the mechanisms

of crazing initiation and propagation into continuum theories for simulating crazing behaviour at the micro- and macroscales. Tijssens et al. (2000) modelled crazes as cohesive surfaces embedded between continuum finite elements. A stress-based crazing initiation criterion, a rate-dependent viscoplastic model for craze propagation, and a failure criterion based on fibril maximum extension were incorporated into the cohesive surface model. Similarly, Socrate et al. (2001) proposed a micromechanical model by introducing craze elements (similar to interface elements) between conventional finite elements for modelling multiple craze formation in High Impact Polystyrene (HIPS). Since the locations of the crazes are not known a priori, a large number of cohesive surfaces or elements have to be used. Instead of capturing each individual craze, a homogenised continuum constitutive model for crazing was developed by Gearing and Anand (2004b), with the inelastic deformation at macroscopic level representing local craze deformations in an average sense. These authors assumed that shear plasticity occurs prior to crazing under tension and that there is a transition from shear yielding to craze yielding which is captured via a change in the flow rule driven by a stress criterion. The craze breakdown and fracture occurs when the craze strain reaches a critical value. In finite element simulations, failure is simulated using an element-removal technique. To address the well-known issues of mesh dependency occurring when using the element-removal technique, this framework was recently modified by Narayan and Anand (2021) using a regularised phase-field model. Since these authors viewed crazing as precursor for fracture, they did not consider the large deformations resulting from crazing beyond the yield point, which limits their range of application. Helbig et al. (2016) developed a micromechanics-based constitutive model for rubber-toughened polymers with distributed crazes. In this model, the inelastic deformation rate accounts for the contributions of both the normal opening and tangential craze opening. The kinetics of craze opening is modelled using phenomenological cohesive law-like formulations (Tijssens et al., 2000). One of the limitation of the model lies in the inability of simulating the scenario under a complex loading condition due to the lack consideration of shear plasticity.

To the best of our knowledge, a comprehensive constitutive model able to predict the large deformation behaviour of glassy polymers by craze yielding and shear plasticity in complex loading scenarios has not yet been proposed. The aim of this paper is to fill this gap by proposing a thermodynamically-consistent constitutive framework that can

describe both shear yielding and craze yielding in glassy polymers. The main assumption of the model is that shear yielding and craze yielding occur exclusively from each other, depending on the value of the local macroscopic stress and based on the underlying mechanisms of shear yielding and crazing. Here, inelastic deformations due to crazing are modelled in a homogenised sense, which allows us to model craze yielding using a formalism similar to shear plasticity but differing in the expressions of the driving force and flow rule. We implemented our theory in the finite element software Abaqus through a user defined material subroutine (UMAT), enabling numerical simulations under complex loading conditions. We validated our model using an extensive set of new experimental data for a commercial grade of purely amorphous polylactic acid (PLA), including compression tests, tension tests, and three point bending tests on plain and notched specimens. We further compared the predictions of our model to experimental data from the literature for another grade of PLA and HIPS. We show that our model is capable of reproducing experimentally-observed phenomena including post-yield softening and drawing to large deformations. The stability of craze yielding-dominated tensile response against necking is highlighted.

The paper is organised as follows. In Section 2, we present the experimental procedure and some key experimental observations in tensile and compression tests on purely amorphous PLA, as well as the main assumptions of our model. Section 3 presents the thermodynamic framework for elastic-inelastic deformation that accounts for both shear plasticity and craze yielding. We introduce the specific forms of the free energy formula and the constitutive models in Section 4. The model is validated against experimental data for amorphous PLA in Sections 6 and 7. The applicability of our model to High-Impact Polystyrene is illustrated in Section 8. Finally, we finish in Section 9 with some concluding remarks.

2. Experimental observations for amorphous PLA and modelling assumptions

2.1. Experimental procedure

We conducted mechanical tests on a commercial grade of purely amorphous PLA (Ingeo 4060D, Natureworks, LLC). The glass transition temperature of this PLA grade is 54 °C, as determined via Dynamic Mechanical Analysis (DMA) at the frequency of 1 Hz in our previous work (Chen et al., 2023). The polymer was purchased in pellet

form and moulded into thick sheets, which were machined into desired specimens shapes: cylindrical specimens for compression testing (height: 4 mm, diameter: 5 mm), dog-bone shape specimens for tensile testing (ISO527 type 1BA with a 2-mm thickness and 25-mm gauge length), and beam specimens (length: 100 mm, height: 5 mm, width: 12.5 mm) for bending tests. Bending specimens were either plain or machined with a semi-circular single edge notch with a 2-mm radius. More details about the processing and manufacturing of the PLA specimens are reported in our previous work (Chen et al., 2023).

All mechanical tests were performed using a commercial screw-driven load frame (Instron 5980) equipped with a 10 kN load cell in an environmental chamber (Instron 3119) at a constant temperature of 37 °C. Compression tests were performed on cylindrical specimens at constant true strain rates of 10^{-3}, 10^{-2} and 10^{-1} s^{-1}. The true compressive stress was calculated as F/A, where F is the force and A the current cross-section area. Neglecting the volume change during elastic deformation, and assuming that the plastic response in compression, dominated by shear yielding, is volume preserving (Argon, 2013), A is estimated as $A = A_0/(1 + \epsilon_y)$, where A_0 is the undeformed cross-section area and ϵ_y is the (negative) nominal strain in the loading direction. Tensile tests were conducted on the dog-bone specimens at constant cross-head velocities of $V_{c-h} = 5 \times 10^{-3}$, 1×10^{-2} and 2×10^{-2} mm s^{-1}. Tensile specimens were spray painted and DIC analysis of the local displacement and strain fields in the gauge region was performed using the commercial software MatchID (MatchID, 2023). The DIC parameters used for generating the figures presented in this work are collected in Table A1. These parameters were selected to achieve a good balance between spatial resolution and noise level, assessed by varying the dimensions of the virtual strain gauge (VSG). As shown in a later section, DIC measurements revealed significant strain heterogeneities within the gauge area. For this reason, the tension response is reported in terms of engineering stress and strain calculated as: F/A_0 and u_{c-h}/L_0, where A_0 is the initial cross-section area in the gauge region, u_{c-h} is the cross-head moving distance, and L_0 is the initial gauge length. For later use, we also introduce the average true strains for the gauge area as: $\bar{\varepsilon}_y = \ln(L/L_0)$ and $\bar{\varepsilon}_x = \ln(D/D_0)$, where L is the deformed gauge length, D and D_0 are the deformed and initial gauge widths, with L and D measured via DIC. Directions x and y are the transverse and longitudinal (loading) directions, respectively. Assuming

isotropic material behaviour so that $\bar{\varepsilon}_x = \bar{\varepsilon}_z$, the average true stress was calculated as: $\bar{\sigma}_y = F/A = (F/A_0)\exp(-2\bar{\varepsilon}_x)$. Further details of the experimental setup for the bending tests will be provided in Section 6.

Specimen surfaces were examined at various loading stages using an Olympus BX51TRF microscope. To this end, additional cubic specimens (side length: 5mm) were tested in compression, since the curved surface of cylindrical specimens is not suitable for microscopy.

2.2. Experimental response in tension and compression

In compression, PLA exhibits the typical response of a glassy polymer, involving elastic deformation, rate-dependent yielding followed by pronounced softening, and a plateau response with limited rehardening (Fig. 1a). Plasticity is mediated by local shear transformations coalescing into shear bands (Fig. 1b). As expected, crazing is not observed under compression. The larger softening response observed for the largest strain rate can be attributed to adiabatic heating, as discussed in (Chen et al., 2023).

The tension response of PLA is shown in Fig. 1c, showing a qualitatively similar response involving an initial elastic response followed by rate-dependent yielding, softening, and a plateau, before failure. Note that post-yield softening is much less pronounced in tension than in compression. Interestingly, the tensile specimens did not show any necking despite the large deformation reached at the point of failure, of almost 20% overall, and the absence of rehardening. Tensile specimens exhibited significant crazing on their surface (Fig. 1d), and we did not see any evidence of shear banding associated with shear plasticity.

In our previous work (Chen et al., 2023), we showed that the inelastic tension response of PLA is dominated by crazing, rather than shear yielding. The key evidence for this is the near absence of lateral contraction during the inelastic portion of the loading, so that the volume change is almost equal to the longitudinal strain. Since shear plasticity is essentially volume preserving, we deduce that the longitudinal deformation is entirely accommodated by crazing. Craze-dominated plasticity also explains the stability of the tensile specimens against necking (G'sell et al., 2002). Local deformation fields measured by DIC in the present experiments will be shown in a later section.

Fig. 2 shows the yield stress (here defined as the peak true stress) as a function of the natural logarithm of the true strain rate at the yield point in both tension and

compression. For the tension response, we used the average true stress $\bar{\sigma}_y$ at the peak as an estimate of the yield stress, and the corresponding average true longitudinal strain rate. This is reasonable considering that, up to the yield point, the strain field is fairly uniform and the strain rate is approximately constant in the gauge area, as confirmed from DIC measurements. The apparent linear relations suggest that both shear plasticity and craze yielding are thermally-activated processes that can be described by an Eyring-type equation with different activation volumes, see also (Chen et al., 2023).

In our experiments for amorphous PLA at body temperature, we always observed craze-dominated yielding under tension, with no evidence of shear yielding. However, it should be acknowledged that glassy polymers may in general undergo shear yielding before crazing, depending on the combination of strain rate and temperature. The transition between crazing and shear plasticity in tension is referred to as the brittle-ductile (BD) transition, or crazing-shearing transition (Haward, 1997; Deblieck et al., 2011; Razavi et al., 2020). More generally, both crazing and shear plasticity can occur simultaneously in neat or rubber-toughened glassy polymers (G'sell et al., 2002; Stoclet et al., 2014; Haward, 1997).

2.3. Modelling assumptions

Based on the above considerations, we develop our constitutive model based on the following assumptions:

- We assume that the material response in tension is dominated by craze yielding, whereas only shear yielding can occur in compression. Our model is thus only valid in the range of temperature and strain rate in which this is the case for a given polymer.

- Shear and craze yielding are both modelled as continuum processes characterised by an inelastic deformation evolving according to a given flow rule. However, flow directions and flow rates are different under shear yielding and crazing. Both, however, can be modelled as thermally-activated processes obeying an Eyring-type equation.

- Adiabatic heating is neglected and the temperature is assumed constant. This holds provided that the loading rate is sufficiently small for the heat generated by inelastic deformation to escape within the timescale of the experiment.

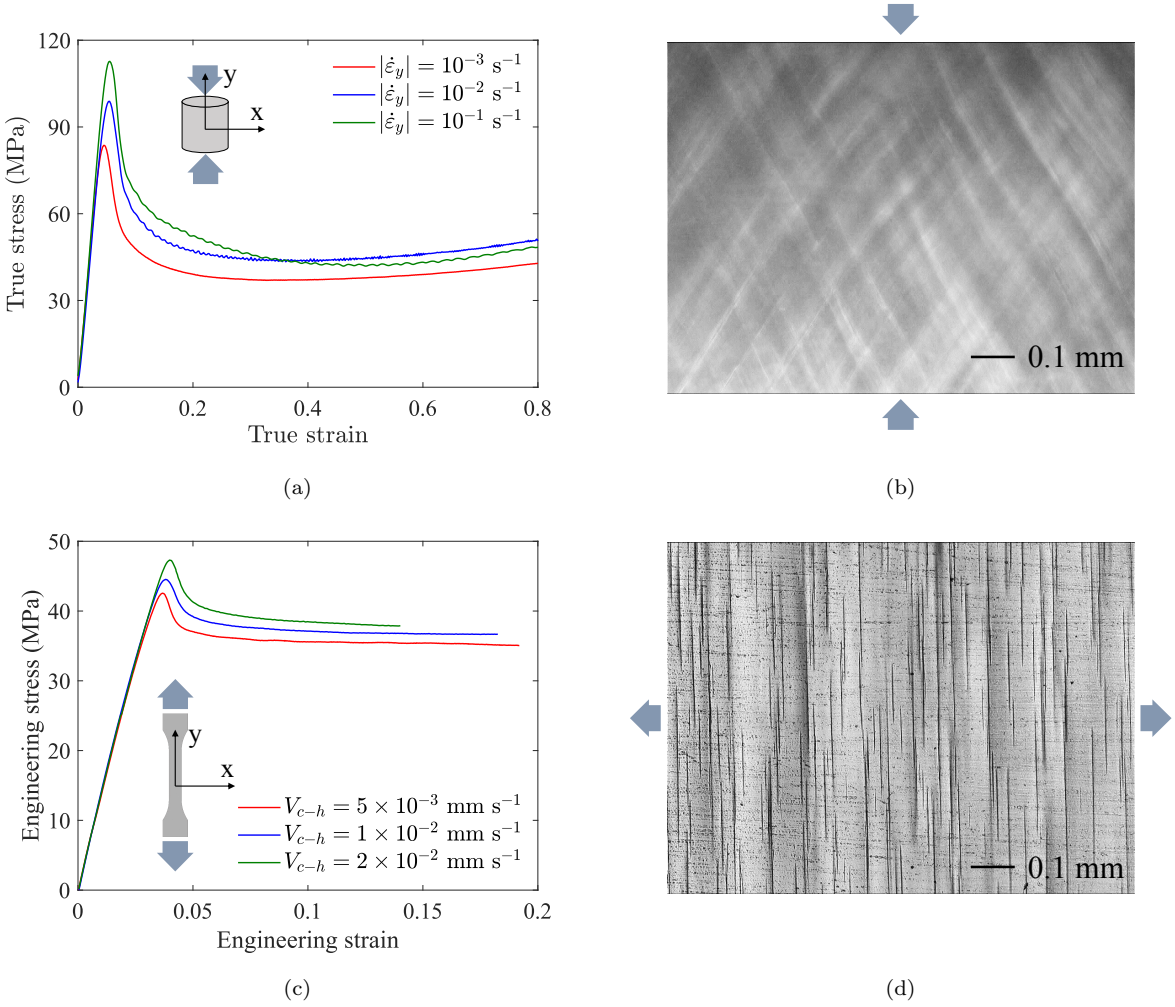

Figure 1: (a) True stress-strain response of PLA 4060D in compression tests at constant true strain rate at 37 °C. The true stress was calculated assuming incompressibility. (b) Micrograph of the centre of a cubic compression specimen taken at the true compression strain of 5×10^{-2}, showing shear banding. (c) Engineering stress-strain response of PLA 4060D in tensile tests at constant cross-head velocity at 37 °C. The engineering strain was calculated based on the cross-head displacement and initial gauge length. (d) Micrograph taken at the centre of the specimen surface at the engineering strain of 5×10^{-2}, showing the crazing pattern.

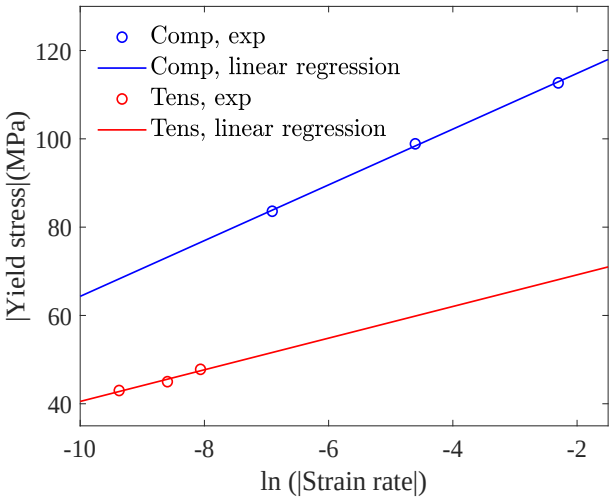

Figure 2: Strain-rate dependence of the yield stress of PLA 4060D at 37 °C in compression and tension. Symbols are experimental data and continuous lines represent linear regressions.

It is emphasised that our model does not seek to describe microstructural details associated with crazing, such as the nucleation and growth of individual crazes, followed by the formation of visible cracks. Instead, our model focuses on the dilatant inelastic deformations emerging at the macroscopic scale, as a result of crazing. These inelastic deformations should be understood as average deformations over a representative volume containing many crazes. This approach has been adopted in several recent studies (Argon, 2013; Venkatesan and Basu, 2015; Narayan and Anand, 2021).

3. Continuum thermodynamic framework

Based on the considerations outlined in the previous section, we formulate a constitutive model for shear plasticity and craze yielding within a thermodynamically-consistent framework in large deformations. The constitutive model is schematically represented in Fig. 3, and consists of a viscoplastic branch and hardening branch in parallel. The viscoplastic branch is composed of a hyperelastic spring and an Eyring-type dashpot, characterising the elastic and rate-dependent plastic behaviours, respectively. The dashpot describes either shear plasticity or craze yielding following a stress-based criterion. The hardening branch consists of a hyperelastic element describing rehardening at large deformation.

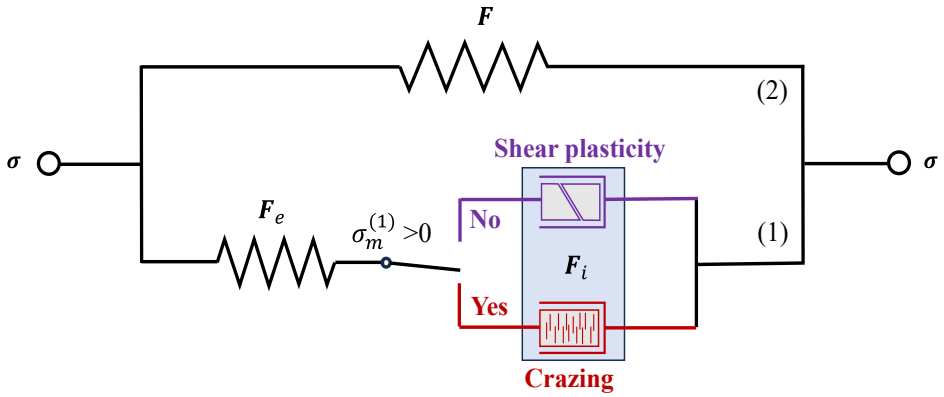

Figure 3: Illustration of the constitutive model using one-dimensional rheological elements.

3.1. Kinematics

Let $\boldsymbol{X}$ denote the position of a material point in the reference state. In the current state, the position of the material point is given by the one-to-one mapping $\boldsymbol{x} = \boldsymbol{x}(\boldsymbol{X}, t)$ where t denotes the time, and the material velocity is $\boldsymbol{v} = \dot{\boldsymbol{x}}$. The relative motion of material points is measured through the deformation gradient:

$$\boldsymbol{F} = \frac{\partial \boldsymbol{x}}{\partial \boldsymbol{X}} \tag{1}$$

We also introduce the Jacobian: $J = \det(\boldsymbol{F}) > 0$.

We regard the local deformation as contributed by elastic distortion and inelastic (plastic) deformation. Following the conventional treatment of elastic-plastic deformation at finite strains (Lee, 1969; Huang et al., 2020), we adopt the multiplicative decomposition of the deformation gradient:

$$\boldsymbol{F} = \boldsymbol{F}_e \boldsymbol{F}_i \tag{2}$$

where $\boldsymbol{F}_e$ and $\boldsymbol{F}_i$ represent the elastic and inelastic contributions to the total deformation gradient, respectively.

3.2. Balance of forces and moments

Consider an arbitrary sub-part of a polymer body subjected to a nominal surface traction $\boldsymbol{T}(\boldsymbol{X}, t)$ and a field of nominal body force $\boldsymbol{B}(\boldsymbol{X}, t)$. Neglecting inertial effects, force balance on the sub-region requires that:

$$\boldsymbol{\nabla} \cdot \boldsymbol{P} + \boldsymbol{B} = \boldsymbol{0} \tag{3}$$

where $\boldsymbol{P}$ is the first Piola-Kirchhoff stress tensor. The first Piola-Kirchhoff stress $\boldsymbol{P}$ tensor and traction vector $\boldsymbol{T}$ are related by Cauchy's relation:

$$\boldsymbol{T} = \boldsymbol{P} \cdot \boldsymbol{N} \tag{4}$$

where $\boldsymbol{N}$ is the outward unit normal vector to a plane in the reference configuration. On the other end, balance of moments requires that $\boldsymbol{P}\boldsymbol{F}^T = \boldsymbol{F}\boldsymbol{P}^T$. We also recall the usual relations between the Cauchy stress tensor and the first Piola-Kirchhoff stress tensor:

$$\boldsymbol{P} = J\boldsymbol{\sigma}\boldsymbol{F}^{-T}, \quad \boldsymbol{\sigma} = J^{-1}\boldsymbol{P}\boldsymbol{F}^T \tag{5}$$

Independent of the activated module (shear plasticity or craze yielding), the total stress tensor can be expressed as the sum of the stresses in the viscoplastic and hardening branches of the respective module:

$$\boldsymbol{P} = \boldsymbol{P}^{(1)} + \boldsymbol{P}^{(2)}, \quad \boldsymbol{\sigma} = \boldsymbol{\sigma}^{(1)} + \boldsymbol{\sigma}^{(2)} \tag{6}$$

where $\boldsymbol{P}^{(1)}$, $\boldsymbol{\sigma}^{(1)}$ and $\boldsymbol{P}^{(2)}$, $\boldsymbol{\sigma}^{(2)}$ are the stresses in the viscoplastic and hardening branches, respectively.

3.3. Free energy imbalance

We regard a sub-part P of polymer as a thermodynamic system. Assuming a constant uniform temperature, thermodynamics requires that the power of the external forces should be larger than the total change in free energy:

$$\frac{d}{dt}\int_P \psi \, dV \leq \int_P \boldsymbol{B} \cdot \boldsymbol{v} \, dV + \int_{\partial P} \boldsymbol{T} \cdot \boldsymbol{v} \, dA \tag{7}$$

where ψ is the (Helmholtz) free energy density of the polymer (energy per unit volume in the reference configuration). In Eq. (7), the first term on the right-hand side is the power of the body forces and the second term is the power of the external tractions. Bringing the time derivative inside the integral, inserting Cauchy's relation (4) and using the divergence theorem, we obtain:

$$\int_P \dot{\psi} dV \leq \int_P \boldsymbol{P} : \dot{\boldsymbol{F}} dV + \int_P (\boldsymbol{\nabla} \cdot \boldsymbol{P} + \boldsymbol{B}) \cdot \boldsymbol{v} \, dV \tag{8}$$

Using the equilibrium condition (3) and requiring the inequality (8) to hold for arbitrarily small volume, we obtain the following local inequality:

$$\boldsymbol{P} : \dot{\boldsymbol{F}} - \dot{\psi} \geq 0 \tag{9}$$

Inserting Eqs. (2) and (6), the stress power is re-expressed as:

$$\boldsymbol{P} : \dot{\boldsymbol{F}} = \boldsymbol{P}_e^{(1)} : \dot{\boldsymbol{F}}_e + \boldsymbol{M}^{(1)} : \boldsymbol{L}_i + \boldsymbol{P}^{(2)} : \dot{\boldsymbol{F}} \tag{10}$$

where the stress-like tensors $\boldsymbol{P}_e^{(1)}$ and $\boldsymbol{M}_i^{(1)}$ are defined as:

$$\begin{aligned} \boldsymbol{P}_e^{(1)} &:= \boldsymbol{P}^{(1)} \boldsymbol{F}_i^T \\ \boldsymbol{M}_i^{(1)} &:= \boldsymbol{F}_e^T \boldsymbol{P}^{(1)} \boldsymbol{F}_i^T \end{aligned} \tag{11}$$

and $\boldsymbol{L}_i$ is the inelastic spatial velocity gradient:

$$\boldsymbol{L}_i = \dot{\boldsymbol{F}}_i \boldsymbol{F}_i^{-1} \tag{12}$$

Using Eq. (10), the dissipation inequality (9) is rewritten as:

$$\boldsymbol{P}_e^{(1)} : \dot{\boldsymbol{F}}_e + \boldsymbol{M}_i^{(1)} : \boldsymbol{L}_i + \boldsymbol{P}^{(2)} : \dot{\boldsymbol{F}} - \dot{\psi} \geq 0 \tag{13}$$

3.4. State laws and reduced inequality

Our theory involves two independent state variables: the total and elastic deformation gradients $\boldsymbol{F}$ and $\boldsymbol{F}_e$. Accordingly, the free energy is taken of the following form $\psi = \psi(\boldsymbol{F}, \boldsymbol{F}_e)$. According to Fig. 3, we further decompose the free energy into two contributions:

$$\psi(\boldsymbol{F}, \boldsymbol{F}_e) = \psi^{(1)}(\boldsymbol{F}_e) + \psi^{(2)}(\boldsymbol{F}) \tag{14}$$

where $\psi^{(1)}$ and $\psi^{(2)}$ denote the free energy due to elastic deformation in the viscoplastic and hardening branches, respectively. The inequality (13) becomes:

$$\left(\boldsymbol{P}_e^{(1)} - \frac{\partial \psi^{(1)}}{\partial \boldsymbol{F}_e}\right) : \dot{\boldsymbol{F}}_e + \left(\boldsymbol{P}^{(2)} - \frac{\partial \psi^{(2)}}{\partial \boldsymbol{F}}\right) : \dot{\boldsymbol{F}} + \boldsymbol{M}_i : \boldsymbol{L}_i \geq 0 \tag{15}$$

This leads to the state laws for the stresses:

$$\boldsymbol{P}_e^{(1)} = \frac{\partial \psi^{(1)}}{\partial \boldsymbol{F}_e}, \quad \boldsymbol{P}^{(2)} = \frac{\partial \psi^{(2)}}{\partial \boldsymbol{F}} \tag{16}$$

Using Eqs. (6) and (11), the stress tensors $\boldsymbol{P}^{(1)}$ and $\boldsymbol{M}_i^{(1)}$ are readily obtained:

$$\boldsymbol{P}^{(1)} = \frac{\partial \psi^{(1)}}{\partial \boldsymbol{F}_e} \boldsymbol{F}_i^{-T}, \ \boldsymbol{M}_i^{(1)} := \boldsymbol{F}_e^T \frac{\partial \psi^{(1)}}{\partial \boldsymbol{F}_e} \tag{17}$$

and the Cauchy stresses $\boldsymbol{\sigma}^{(1)}$ and $\boldsymbol{\sigma}^{(2)}$ are obtained from Eq. (5):

$$\boldsymbol{\sigma}^{(1)} = \frac{1}{J} \frac{\partial \psi^{(1)}}{\partial \boldsymbol{F}_e} \boldsymbol{F}_e^T, \ \boldsymbol{\sigma}^{(2)} = \frac{1}{J} \frac{\partial \psi^{(2)}}{\partial \boldsymbol{F}} \boldsymbol{F}^T \tag{18}$$

The inequality (13) then reduces to:

$$\boldsymbol{M}_i^{(1)} : \boldsymbol{L}_i \geq 0 \tag{19}$$

Following (Doghri, 2000; Reese and Govindjee, 1998), Eq.(19) can be rewritten as:

$$\boldsymbol{\tau}^{(1)}\boldsymbol{b}_e^{-1} : \left(\boldsymbol{F}_e\boldsymbol{L}_i\boldsymbol{F}_e^T\right) \geq 0 \tag{20}$$

where $\boldsymbol{\tau}^{(1)} = J\boldsymbol{\sigma}^{(1)}$ is the Kirchhoff stress tensor, and $\boldsymbol{b}_e$ is the elastic left Cauchy-Green tensor: $\boldsymbol{b}_e = \boldsymbol{F}_e\boldsymbol{F}_e^T$. Further, $\boldsymbol{F}_e\boldsymbol{L}_i\boldsymbol{F}_e^T$ can be split into a symmetric and skew-symmetric parts as:

$$\boldsymbol{F}_e\boldsymbol{L}_i\boldsymbol{F}_e^T = -\frac{1}{2}\underbrace{\left(\boldsymbol{F}\dot{\boldsymbol{C}}_i^{-1}\boldsymbol{F}^T\right)}_{\mathcal{L}_v\boldsymbol{b}_e} + \text{skew}\left(\boldsymbol{F}_e\boldsymbol{L}_i\boldsymbol{F}_e^T\right) \tag{21}$$

where we identified the Lie derivative of the left Cauchy-Green tensor $\boldsymbol{b}_e$:

$$\mathcal{L}_v\boldsymbol{b}_e = \boldsymbol{F}\left(\frac{D(\boldsymbol{F}^{-1}\boldsymbol{b}_e\boldsymbol{F}^{-T})}{Dt}\right)\boldsymbol{F}^T = \left(\boldsymbol{F}\dot{\boldsymbol{C}}_i^{-1}\boldsymbol{F}^T\right) \tag{22}$$

corresponding to the push forward of the rate of inelastic deformation tensor $\dot{\boldsymbol{C}}_i^{-1}$ to the current configuration with $\boldsymbol{C}_i = \boldsymbol{F}_i^T\boldsymbol{F}_i$ (Simo and Hughes, 2006).

Then, we make the conventional assumption that the plastic flow is irrotational, i.e. $\text{skew}(\boldsymbol{F}_e\boldsymbol{L}_i\boldsymbol{F}_e^T) = \boldsymbol{0}$, which finally leads to the reduced equality:

$$-\boldsymbol{\tau}^{(1)} : \frac{1}{2}(\mathcal{L}_v\boldsymbol{b}_e)\boldsymbol{b}_e^{-1} \geq 0 \tag{23}$$

Further, it can be shown that the trace of $-\frac{1}{2}(\mathcal{L}_v\boldsymbol{b}_e)\boldsymbol{b}_e^{-1}$ equals the logarithmic inelastic volumetric strain rate $\dot{\epsilon}_i^v$ (Doghri, 2000):

$$\text{tr}\left(-\frac{1}{2}(\mathcal{L}_v\boldsymbol{b}_e)\boldsymbol{b}_e^{-1}\right) = \frac{d}{dt}(\ln J_i) = \dot{\epsilon}_i^v \tag{24}$$

where $J_i = \det(\boldsymbol{F}_i)$.

Kinetic models for the inelastic flow should be such that the inequality (23) is satisfied.

4. Specific constitutive models

4.1. Free energy function

We assume that the free energy functions for shear plasticity and craze yielding take the same general form and only differ in the specific choice of the material constants.

Branch (1) of the model describes intermolecular interactions. Considering that the elastic deformation resulting from intermolecular interactions is small, the free energy

function $\psi^{(1)}$ of the viscoplastic branch is taken of the form (Anand, 1985; Anand et al., 2012):

$$\psi^{(1)}\left(\boldsymbol{F}_e\right)=\bar{\psi}^{(1)}\left(\varepsilon_{e,1},\varepsilon_{e,2},\varepsilon_{e,3}\right)=G^{(1)}\mathrm{tr}\left(\boldsymbol{E}_e^2\right)+\frac{\lambda^{(1)}}{2}\left(\mathrm{tr}\boldsymbol{E}_e\right)^2 \tag{25}$$

where $\varepsilon_{e,i}=\ln(\lambda_{e,i}), i=1,2,3$ are the principal elastic logarithmic strains, i.e, the eigenvalues of the elastic logarithmic strain tensor $\boldsymbol{E}_e=\ln(\boldsymbol{U}_e)=\ln(\sqrt{\boldsymbol{F}_e^T\boldsymbol{F}_e})$, $\lambda_{e,i}$ are the principal elastic stretches, $G^{(1)}$ and $\lambda^{(1)}$ are respectively the first and second Lamé constants.

The strain energy stored in branch (2) is attributed to the reduction of entropy due to stretching and aligning the polymer chains at large deformation. Here it is described using a compressible Neo-Hookean model (Horgan and Saccomandi, 2004):

$$\psi^{(2)}\left(\boldsymbol{F}\right)=\bar{\psi}^{(2)}\left(I_1\left(\boldsymbol{C}_e\right),I_3\left(\boldsymbol{F}_e\right)\right)=\frac{G^{(2)}}{2}\left(I_1-3-2\ln J\right)+\frac{\lambda^{(2)}}{2}\left(\ln J\right)^2 \tag{26}$$

where $G^{(2)}$ and $\lambda^{(2)}$ are respectively the first and second Lamé constants. In what follows, we add subscripts p and c to the Lamé constants to distinguish between shear plasticity and craze yielding when necessary.

Inserting Eqs (25) and (26) into Eq. (18), we obtain the specific expressions for stresses:

$$\boldsymbol{\sigma}^{(1)}=\frac{1}{J}\left[2G^{(1)}\left(\mathrm{dev}\boldsymbol{E}_e\right)+K^{(1)}\left(\mathrm{tr}\boldsymbol{E}_e\right)\boldsymbol{1}\right] \tag{27}$$

$$\boldsymbol{\sigma}^{(2)}=\frac{G^{(2)}}{J}\left(\boldsymbol{b}-\boldsymbol{1}\right)+\frac{\lambda^{(2)}}{J}\left(\ln J\right)\boldsymbol{1} \tag{28}$$

4.2. Switch criterion for shear plasticity and craze yielding

At microscale, crazing initiates on the planes normal to the direction of maximum tensile principal stress (Bucknall, 2007b; Argon, 2013; Haward, 1997), and are expanded under a positive mean stress (Argon, 2013). Based on this physical picture, we adopt the following simple criterion for the onset of craze yielding at macroscopic scale: that both the first principal stress σ_1 and the mean stress σ_m should be positive. These two conditions can be merged into a single condition: $\sigma_m>0$ (since a positive mean stress implies a positive first principal stress). The adopted switch criterion is thus very simple: if $\sigma_m>0$, craze yielding occurs, otherwise shear plasticity occurs.

4.3. Flow rule for shear plasticity

We assume that shear yielding is volume preserving and adopt a von Mises-based flow rule (Mises, 1913; de Souza Neto et al., 2011):

$$-\frac{1}{2}(\mathcal{L}_v \boldsymbol{b}_e)\boldsymbol{b}_e^{-1} = \dot{\gamma}_p \boldsymbol{N}_p \tag{29}$$

where $\dot{\gamma}_p$ denotes the equivalent plastic strain rate in shear plasticity and $\boldsymbol{N}_p$ specifies the flow direction and is given by:

$$\boldsymbol{N}_p = \frac{\tilde{\boldsymbol{\tau}}^{(1)}}{\sqrt{2}\tau^{(1)}},\ \tau^{(1)} = \sqrt{\frac{1}{2}\tilde{\boldsymbol{\tau}}^{(1)} : \tilde{\boldsymbol{\tau}}^{(1)}} \tag{30}$$

where $\tilde{\boldsymbol{\tau}}^{(1)} = \text{dev}\ \boldsymbol{\tau}^{(1)}$ denotes the deviatoric part of the stress tensor $\boldsymbol{\tau}^{(1)}$, so that $\text{tr}(\boldsymbol{N}_p) = 0$.

Combining Eqs. (24), (29), and (30), we therefore have that: $\dot{\epsilon}_i^v = 0$, i.e. plastic deformation is volume preserving. Many forms of $\dot{\gamma}_p$ have been proposed in the literature, either suggested through molecular yield theories with each assuming a different molecular rearrangement or conformational change (Eyring, 1936; Robertson, 1966; Argon, 1973a) or based on shear transformation zones theory (Argon, 1979; Voyiadjis and Samadi-Dooki, 2016; Chevalier et al., 2018; Van Loock et al., 2021; Lin et al., 2023). Here we adopt the Eyring-type equation modified by Govaert et al. (2000) to describe the stress-activated flow rate:

$$\dot{\gamma}_p = \dot{\gamma}_p^r \text{exp}\left(-\frac{\Delta G_p}{k_B T} + H_p\right) \text{sinh}\left(\frac{\tau^{(1)} V_p}{k_B T}\right) \tag{31}$$

where $\dot{\gamma}_p^r$ is a reference flow rate, ΔG_p denotes activation energy for viscoplastic flow, H_p is history variable introduced for considering post-yield softening, k_B is the Boltzmann constant, T is the absolute temperature, and V_p represents the activation volume.

For modelling post-yield softening response, following Boyce et al. (1988), a phenomenological evolution function for H_p is used:

$$\dot{H}_p = h_p \left(1 - \frac{H_p}{H_p^s}\right) \dot{\gamma}_p,\ H_p(0) = 0 \tag{32}$$

where h_p and H_p^s are softening parameters related to the softening slope and steady-state yield strength, respectively. It should be noted that H_p^s is generally dependent on temperature and strain rate (Boyce et al., 1988). For simplicity, H_p^s is regarded as a constant in the present study.

4.4. Flow rule for craze yielding

We propose the following form of the flow rule for craze yielding:

$$-\frac{1}{2}(\mathcal{L}_v \boldsymbol{b}_e)\boldsymbol{b}_e^{-1} = \dot{\gamma}_c \boldsymbol{N}_c \tag{33}$$

where $\dot{\gamma}_c$ denotes the crazing strain rate; $\boldsymbol{N}_c$ specifies the crazing direction of flow and can be defined according to (Gearing and Anand, 2004b) as:

$$\boldsymbol{N}_c = \boldsymbol{n}_1 \otimes \boldsymbol{n}_1 \tag{34}$$

where $\boldsymbol{n}_1$ is the eigenvector corresponding to the largest eigenvalue of the stress tensor $\boldsymbol{\tau}^{(1)}$, i.e. the direction of maximum principal stress $\tau_1^{(1)}$. Note that $\boldsymbol{\tau}$ and $\boldsymbol{b}_e$ share the same eigenvector for isotropic materials (de Souza Neto et al., 2011). Combining Eqs. (24), (33), and (34) leads to $\dot{\epsilon}_i^v = \dot{\gamma}_c \geq 0$, showing an increase in volume when $\tau_1^{(1)} > 0$.

We modify the Eyring-type equation using the maximum principal stress of $\boldsymbol{\tau}$ as the activation stress for the crazing flow rate:

$$\dot{\gamma}_c = \dot{\gamma}_c^r \exp\left(-\frac{\Delta G_c}{k_B T} + H_c\right) \sinh\left(\frac{\tau_1^{(1)} V_c}{k_B T}\right) \tag{35}$$

where $\dot{\gamma}_c^r$ is a reference crazing flow rate. ΔG_c denotes activation energy for crazing flow, H_c is history variable introduced for considering post-yield softening, and V_c represents the activation volume for crazing.

It is essential to acknowledge that, as the existing studies (Sternstein and Ongchin, 1969; Narayan and Anand, 2021), our model is not able to handle the particular scenario or equal-biaxial tension, because the flow rule assumes a unique principal stress direction. Physically, it is unclear how crazes would develop under equal-biaxial tension. More research is required to clarify this point and how to appropriately model it.

An evolution function is also introduced for modeling post-softening response under craze yielding:

$$\dot{H}_c = h_c \left(1 - \frac{H_c}{H_c^s}\right) \dot{\gamma}_c, \;\; H_c(0) = 0 \tag{36}$$

where h_c and H_c^s are softening parameters related to the softening slope and steady-state crazing stress, respectively.

5. Numerical algorithm and implementation

We implemented the constitutive model in Abaqus as a user-defined subroutine (UMAT). The numerical implementation requires the update of state variable $\boldsymbol{b}_e$ through the evolution functions (29) for shear plasticity and (33) for craze yielding. The evolution

functions are rewritten in terms of the logarithmic strain through exponential mapping, and are solved using a classical elastic-predictor/plastic-corrector two-step algorithm (de Souza Neto et al., 2011). Further, the return-mapping equation system can be reduced into an equation containing only one scalar unknown $\dot{\gamma}_p$ for shear plasticity and $\dot{\gamma}_c$ for craze yielding, which significantly reduces the computational complexity. We solve the resulted scalar equations using fully implicit algorithm with the Newton-Raphson method. For the numerical implementation of the as a UMAT, Abaqus requires the calculation of the consistent tangent modulus (DDSDDE) needed for the global Newton iterations. We present the details about the numerical algorithm and implementation in Appendix B.

We have verified that the intrinsic strain softening in our constitutive model does not lead to mesh size dependency. This is attributed to the rate-dependence of the model, which inherently introduces a characteristic length scale into the governing equations, even though the constitutive model does not have a length scale (Needleman, 1988; Bazant and Jirásek, 2002; Simo et al., 1993).

6. Application to fully amorphous PLA

We illustrate the model capability by comparing numerical predictions to our experimental data for the fully amorphous PLA grade considered in Section 2. Experimental data include results of uniaxial compression and tensile tests, as well as bending experiments.

6.1. Uniaxial compression tests

We first consider the response of PLA in uniaxial compression tests at constant true strain rates of 10^{-3}, 10^{-2}, and 10^{-1} s^{-1}, described in Section 2. In compression, the mechanical response involves only plastic yielding, and we assume that deformation is homogeneous so that the stress-strain response can be simulated for a single material point.

The model parameters were identified in the following way. The Young modulus E was determined by the slope of the experimental true stress-strain curves, giving $E = 2800$ MPa. The Poisson's ratio ν was identified based on the longitudinal and transverse strain fields in tensile specimens measured by DIC, as explained in the next section. The moduli $G^{(1)}$ and $\lambda^{(1)}$ were then obtained from the classical formulas: $G^{(1)} = \frac{E}{2(1+\nu)}$ and $\lambda^{(1)} = \frac{E\nu}{(1+\nu)(1-2\nu)}$, respectively. The viscoplastic parameter $\frac{V_p}{k_B T}$ was obtained from the

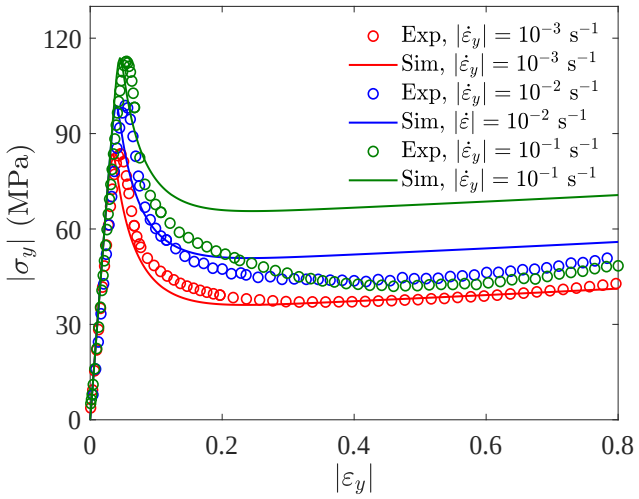

Figure 4: Comparison of model predictions to experimental data for PLA 4060D under uniaxial compression at different true strain rates at 37 °C.

strain-rate dependence of the apparent yield point $|\sigma_y|_Y$ reported in Fig. 2. These data were fitted by the following expression based on Eq. (31):

$$|\sigma_y|_Y = \frac{\sqrt{3}}{V_p/k_BT}\left(\ln|\dot{\epsilon}_y| + \frac{\Delta G_p}{k_BT} - \ln\dot{\gamma}_p^r + \ln\sqrt{6}\right) \tag{37}$$

Here, we neglected the elastic volume change, and we also assumed that $H_p \approx 0$ at the yield point. The reference plastic strain rate $\dot{\gamma}_p^r$ was arbitrarily set to $\dot{\gamma}_p^r = 1$ s^{-1}. The parameters $\frac{V_p}{k_BT}$ and $\frac{\Delta G_p}{k_BT}$ were then identified. The remaining parameters related to softening and rehardening were obtained by fitting the stress strain curve under the strain rate of 10^{-3} s^{-1}. The same parameters were then used to predict the curves at the other strain rates. All the parameters are collected in Table 1.

The comparison between experimental stress-strain curves and model predictions is shown in Fig. 4. The model is capable of providing reasonable predictions for strain rates of 10^{-3} and 10^{-2} s^{-1}. However, it notably overestimates the experimental post-yield response for the strain rate of 10^{-1} s^{-1} due to the omission of adiabatic heating effects in our model. Also, both the model predictions and experimental data show a relatively flat post-yield plateau with limited rehardening. We have verified that using a hyperelastic model with rehardening (i.e. the Gent model, (Gent, 1996)) for the stretching energy does not appreciably change the predictions.

6.2. Uniaxial tensile tests

We next consider the uniaxial tensile tests carried out on dog-bone specimens and described in Section 2. Force-displacement curves are shown in Fig. 5a. Fig. 5b shows the time-evolution of the total longitudinal and volumetric strain in the gauge area ($\bar{\varepsilon}_v = \bar{\varepsilon}_y + 2\bar{\varepsilon}_x$). Since the experiments were conducted at constant cross-head velocity, the total true strain rate $\bar{\varepsilon}_y$ is not constant but increases after the yield point, which corresponds to the change in slope. Simultaneously, the rate of volume change also increases and becomes similar to the rate of longitudinal strain. The drastic increase in volume change observed past the yield point is an evidence of crazing.

The local strain field measured by DIC is found to be homogeneous before yield point in the gauge area, and becomes highly inhomogeneous after the yield point, showing a pattern of bands where the longitudinal strain localises, Fig. 5c. The strain heterogeneity is attributed to the post-yield softening in tension, which causes the strain to localise in regions of higher stress triggered by geometric or material imperfections. However, the observed pattern of strain localisation is different from necking, as it is not accompanied by localised transverse contraction. Note that slightly slanted color borders are observed in the DIC results, which is ascribed to a probable slight misalignment between the loading direction and the specimen introduced during clamping. However, we have verified that this effect has no impact on the macroscopic force-extension response based on repeated tests.

We simulated the tensile response using FE simulations of the dog-bone shape specimens. The illustration of the FEM model is shown in Fig. 6. The geometry was discretised using 3864 C3D8 elements, corresponding to an average element size of 0.625 mm. We have verified that the number of elements is sufficient to obtain converged results. We assumed that the heterogeneous deformations observed in the experiments were triggered by geometric imperfections in the specimens. Accordingly, we applied a random perturbation $\delta = \Delta/h \in [-5, 5] \times 10^{-3}$ to the coordinates of each node on the boundary of the gauge area, where δ is the normalised perturbation, Δ is the absolute perturbation, and h is the thickness of the specimen. As for the boundary conditions, all the degrees of freedom of the bottom surface are fixed. A vertical displacement with cross-head velocities of 5×10^{-3}, 1×10^{-2} and 2×10^{-2} mm s^{-1} was applied on the top surface while keeping the other degrees of freedom fixed. The force was obtained by summing the reaction forces

along the direction y at each node on the top surface. The overall true longitudinal and transverse strains were obtained from the overall changes in dimensions of the gauge area.

Material parameters describing the tension response (craze yielding) were identified as follows. The elastic modulus E was taken the same as in compression. The Poisson's ratio was calculated based on the relationship between the total longitudinal and volumetric strain in the elastic region (Fig. 5b) according to the formula $\bar{\varepsilon}_v = (1-2\nu)\bar{\varepsilon}_y$, giving the value $\nu = 0.35$, which agrees with literature values, e.g. (Farah et al., 2016). The crazing flow parameter $\frac{\Delta G_c}{k_B T}$ was identified from the strain-rate dependency of the yield stress, Fig. 2, similar to the compression case. Remaining parameters were fitted on the experimental data for 5×10^{-3} mm s^{-1}. The same parameters were then used for predicting the experimental results of the other loading rates. Numerical values of all parameters are collected in Table 1. Corresponding true stress-strain curves under the same loading rates as in the compression tests (Fig. 4) are shown in Fig. C.16. By comparing Fig. 4 and Fig. C.16, it is obvious that the tensile yield stress is considerably lower than the compressive yield stress for the same loading rate. Furthermore, the post-yield stress drop is markedly less pronounced in tension, compared to compression.

Model predictions for dog-bone tensile tests are compared to experimental data in Fig. 5. The model well captures the force-displacement response at various cross-head velocities (Fig. 5a), as well as the average longitudinal and volume change in the gauge are (Fig. 5b). Furthermore, the model is also able to capture the striped distribution of longitudinal strain in the gauge region measured by DIC (Fig. 5c), showing generally good agreement. While the magnitude of the longitudinal strain increases with the applied load within the localisation band, these bands do not cause necking of the specimen due to the absence of lateral contraction during crazing. For comparison, we have also simulated the dog-bone tensile test using the shear plasticity model, which as expected, resulted in necking (results not shown). This further confirms that the tensile response of purely amorphous PLA is dominated by craze yielding, rather than shear plasticity.

Fig. 7a shows the time evolution of the local longitudinal strain at different points of the gauge area as measured by DIC. Experimental results confirm the absence of unloading outside the region of strain localisation, which would be expected in necking. Instead, the axial strains at each location consistently continues to increase. These trends are well captured by the FE model (Fig. 7b). In Fig. 7c, we report the local volumetric strain as

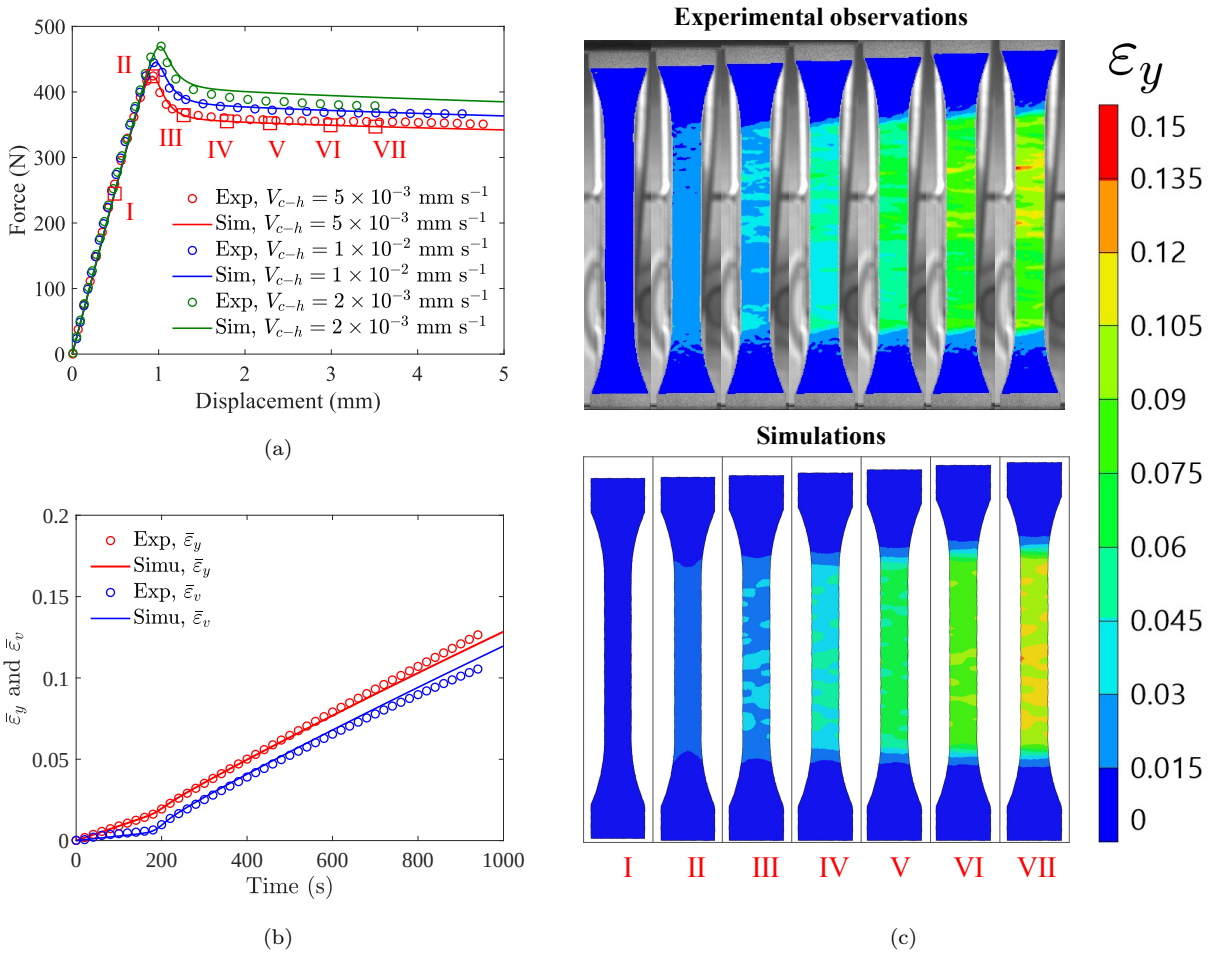

Figure 5: Comparison of model predictions to experimental data for PLA 4060D under uniaxial tension at difference cross-head velocities. (a) Load-displacement curves. (b) Time evolution of the average longitudinal and volumetric strains in the gauge area under a cross-head velocity of 5×10^{-3} mm s^{-1}. (c) Contours of local longitudinal strains under a cross-head velocity of 5×10^{-3} mm s^{-1} at displacements of 0.50, 0.93, 1.30, 1.80, 2.30, 3.0, and 3.5 mm.

a function of the local axial strain. This shows that crazing-induced dilatational plasticity accounts for almost all of the axial deformation at all points.

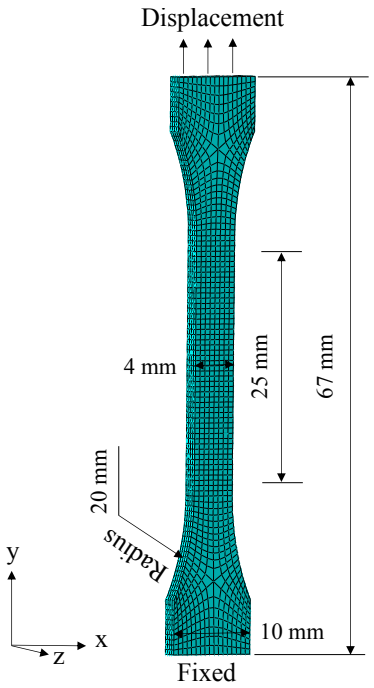

Figure 6: Illustration of the FEM model of a PLA dog-bone tensile specimen.

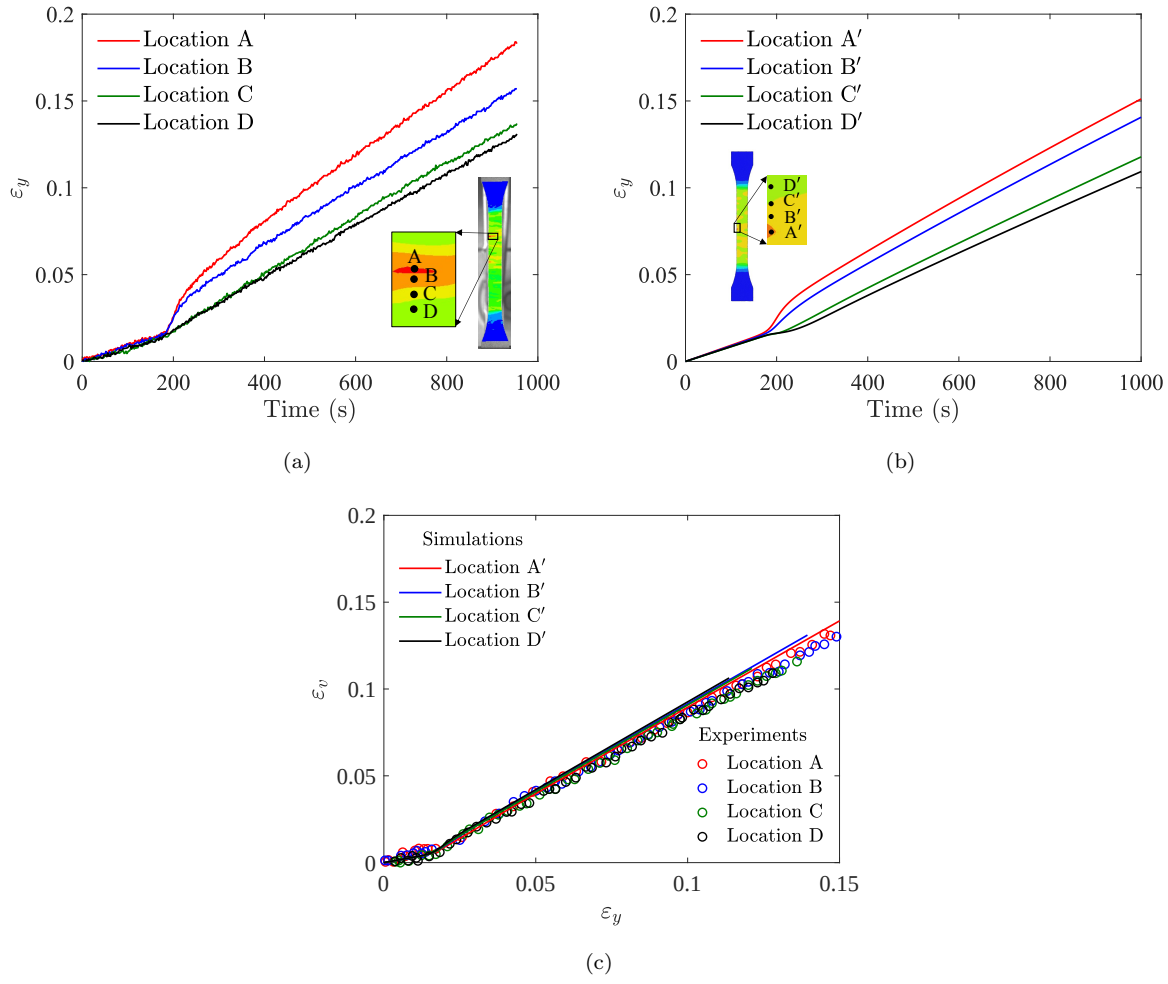

Figure 7: Time evolution of the longitudinal strain at different points of the gauge area in (a) experimental and (b) FE simulations. (c) Local volumetric strain at different points of the gauge area as a function of the local longitudinal strain.

6.3. Bending tests

In the preceding examples, the deformation mechanism was either shear plasticity or craze yielding. In this section, we validate our model in a three-point bending situation where both mechanisms occur simultaneously in different locations of the specimen.

We conducted three-point bending experiments on a PLA beam with dimensions reported in the inset of Fig. 8. The width of the beam was 12.5 mm and the loading speed was 0.1 mm s^{-1}. In the FE simulation, the geometry was discretised using 600 C3D8 elements. Only one quarter of the beam was represented and symmetric boundary conditions were applied on the middle cross-sections perpendicular to the length (x-axial) and width (z-axial) directions. The supports were modelled as discrete rigid bodies with hard contact for the normal behaviour and a penalty friction formulation with friction coefficient of 0.15 for the tangential response. A line displacement was applied on the top surface at points on the symmetry line. The magnitude of the total force was twice that of the reaction force in the loading direction at the support.

In the simulation, we used the complete model where the behaviour switches from shear plasticity-dominated to crazing-dominated deformation depending on the local value of the stress. For comparison, we also carried out simulations where the shear plasticity model is used for both the tension and the compression responses. Fig. 8 compares the load-displacement curves measured experimentally and predicted by the model. The complete model accounting for both deformation mechanisms can reasonably well predict the overall load-displacement response, although it slightly overestimates the post-yielding behaviour. In contrast, when the model only accounts for shear plasticity, the predictions significantly overestimate the yield point and exhibit a much steeper post-yield softening than that observed in the experiments.

The formation of crazes and shear bands within the polymer induces a modification in the refraction index of the material, resulting in a darkening of the affected areas. This can be used to qualitatively compare experimental predictions to experimental data. Fig. 9a presents the photographs of the three-point bending test at different deformation stages. Crazing initially manifests on the bottom surface and then progresses through the thickness and along the longitudinal directions. In contrast, shear bands initiate later than the crazes and occupy smaller areas. This phenomenon arises from the fact that the shear yield stress is larger than the crazing yield stress under the same absolute loading rate, see

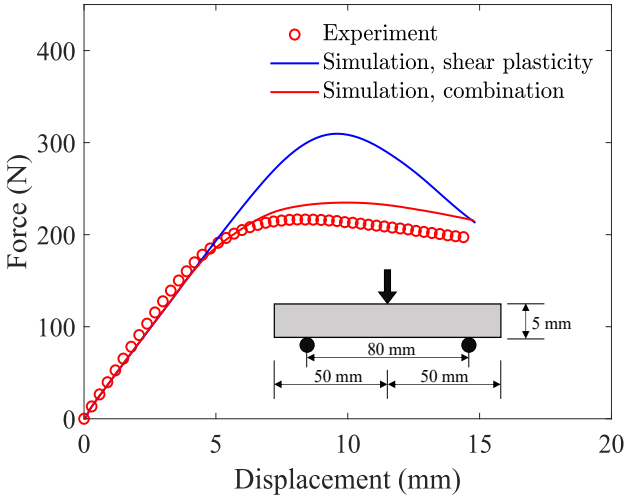

Figure 8: Comparison between the load-displacement curves predicted by FE simulations and experimental data in a three-point bending test of PLA 4060D at the displacement speed of 0.1 mm s^{-1}. A schematic of the bending test is shown in the inset.

Fig. 2. Predicted accumulated inelastic strains resulting from craze yielding $\gamma_c = \int_0^t \dot{\gamma}_c dt'$ and shear plasticity $\gamma_p = \int_0^t \dot{\gamma}_p dt'$ are shown in Fig. 9b and c, respectively, showing good qualitative agreement with the experiments. Furthermore, Fig. 9d illustrates the true volumetric strain. As anticipated, the lower region experiences a significant volume increase due to crazing, while the upper surfaces only undergo a slight volume decrease under compression owing to the elastic deformation.

6.4. Notched bending test

We also conducted three-point bending tests on a notched PLA beam with same overall dimensions as those in Section. 6.3. A semicircular notch with a radius of 2 mm was machined at the bottom of the beam. The setup is shown the inset of Fig. 10. In the simulation, only one quarter of the geometry was considered. The geometry was discretised using 709 C3D8 elements. Other simulation details are the same as in Section 6.3.

Fig. 10 compares the experimentally measured load-displacement curves to those predicted by a model considering only shear plasticity and those predicted by the complete model considering shear plasticity and craze yielding. The complete model incorporating both deformation mechanisms predicts the overall load-displacement behaviour reasonably well. In contrast, similar to the bending test on plain samples, the model that only considers shear plasticity substantially overestimates the yield point and demonstrates a

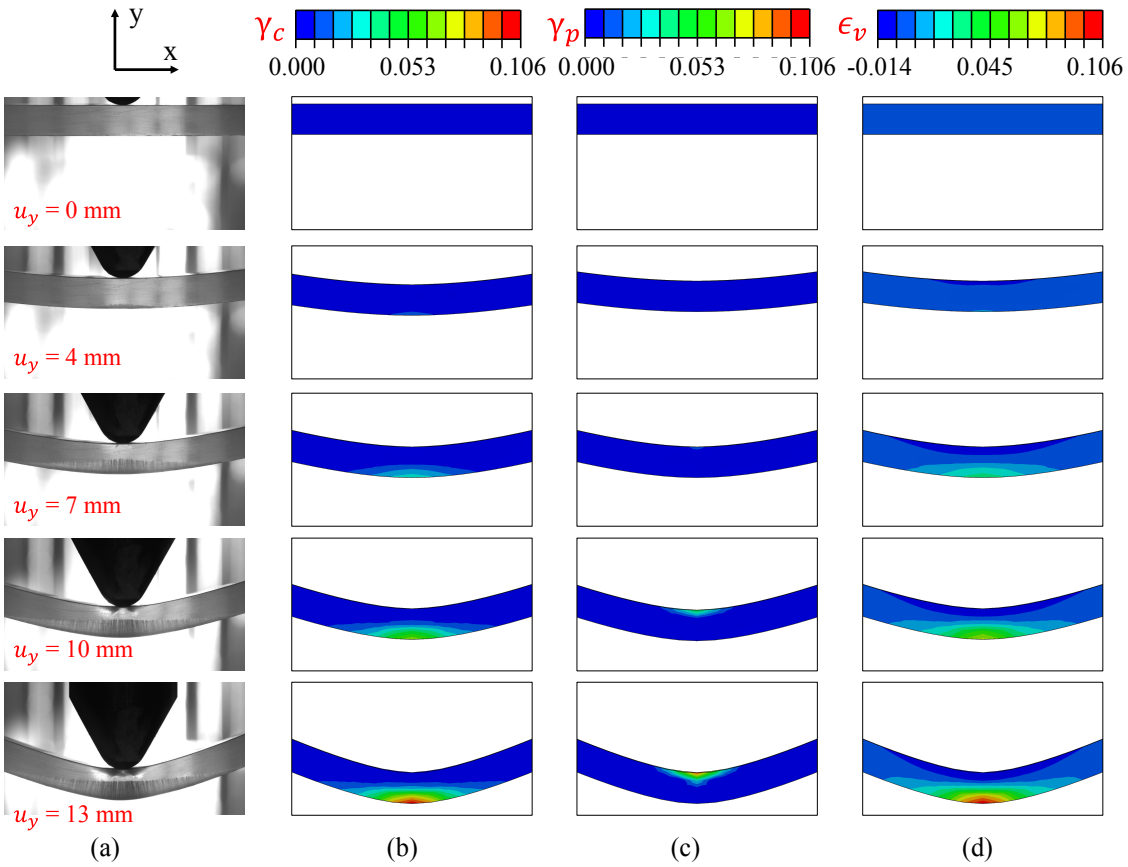

Figure 9: (a) Photographs of the three-point bending test at different values of the applied displacement u_y. FE simulation predictions of the (b) accumulated crazing strain γ_c , (c) accumulated shear plastic strain γ_p, and (d) true volumetric strain ε_v at the same loading stages.

much steeper post-yield softening than that observed in the experiments.

Fig. 11a presents the photographs of the notched bending test at different deformation stages. Crazing first appears at the notch root and then propagates outwards with the frontier of the crazing region showing a round shape. In contrast, shear bands develop much later than the crazes and cover smaller regions at the top of the specimen. The predicted accumulated inelastic strains due to craze yielding and shear plasticity are shown in Fig. 11b and c, respectively, showing good qualitative agreement with the experimental observations. Note that the maximum strain was set to 0.05 in the contour plots of Figs 11b and c (i.e. regions with γ_c and γ_p greater than 0.05 all appear in red) in order to capture the evolution of the accumulated inelastic strains at early deformation stages. Additionally, Fig. 11d shows the true volumetric strains. As expected, the notch root area undergoes substantial volume expansion due to craze yielding, while minimal volume changes occur on the upper surfaces.

Previous studies have explored the competition between the formation of shear bands and crazing on notched tests through numerical modelling (Lai and Van der Giessen, 1997; Estevez et al., 2000; Guo et al., 2015) and experiments (Ishikawa et al., 1977; Narisawa and Yee, 2006; Gearing and Anand, 2004a). In particular, previously-reported results for notched bending of polycarbonate show that shear yielding occurs first at the notch root then crazes initiate in the unyielded region near the tip of the plastic deformation zone (Ishikawa et al., 1977; Gearing and Anand, 2004a). Interestingly, our results shown in Fig. 12 reveal that crazes initiate at the notch root without observable shear bands, suggesting that crazing occurs before shear yielding in this PLA and that craze yielding is the dominating deformation mechanism in tension.

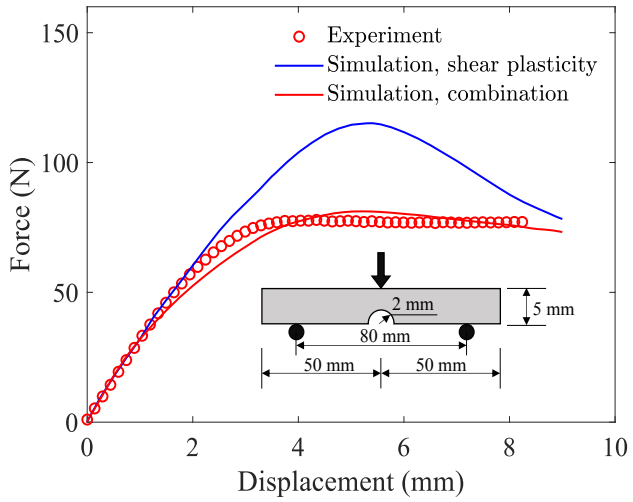

Figure 10: Comparison between the load-displacement curves predicted by FE simulations and experimental data in a notched bending test of PLA 4060D at the displacement speed of 0.1 mm s^{-1}. A schematic of the bending test is shown in the inset.

Table 1: Material parameters for PLA 4060D

Parameter	Unit	Value	Physical significance
$G^{(1)}$	MPa	1040	Shear modulus
$\lambda^{(1)}$	MPa	2420	Lamé's first parameter
$G_c^{(2)}$	MPa	11	Shear modulus of hardening branch for craze yielding
$\lambda_c^{(2)}$	MPa	0.011	Lamé's first parameter of hardening branch for craze yielding
h_c	-	700	Softening parameter relating to the softening slope for craze yielding
H_c^s	-	3.2	Softening parameter relating to the steady yield strength for craze yielding
$\dot{\gamma}_c^r$	s^{-1}	1	Reference flow rate for craze yielding
$\frac{\Delta G_c}{k_B T}$	-	21.7	Normalised activation energy for craze yielding
$\frac{V_c}{k_B T}$	MPa^{-1}	0.286	Normalised activation volume for craze yielding
$G_p^{(2)}$	MPa	4	Shear modulus of hardening branch for shear plasticity
$\lambda_p^{(2)}$	MPa	64	Lamé's first parameter of hardening branch for shear plasticity
h_p	-	150	Softening parameter relating to the softening slope for shear plasticity
H_p^s	-	8.5	Softening parameter relating to the steady yield strength for shear plasticity
$\dot{\gamma}_p^r$	s^{-1}	1	Reference flow rate for shear plasticity
$\frac{\Delta G_p}{k_B T}$	-	19.9	Normalised activation energy for for shear plasticity
$\frac{V_p}{k_B T}$	MPa^{-1}	0.274	Normalised activation volume for shear plasticity

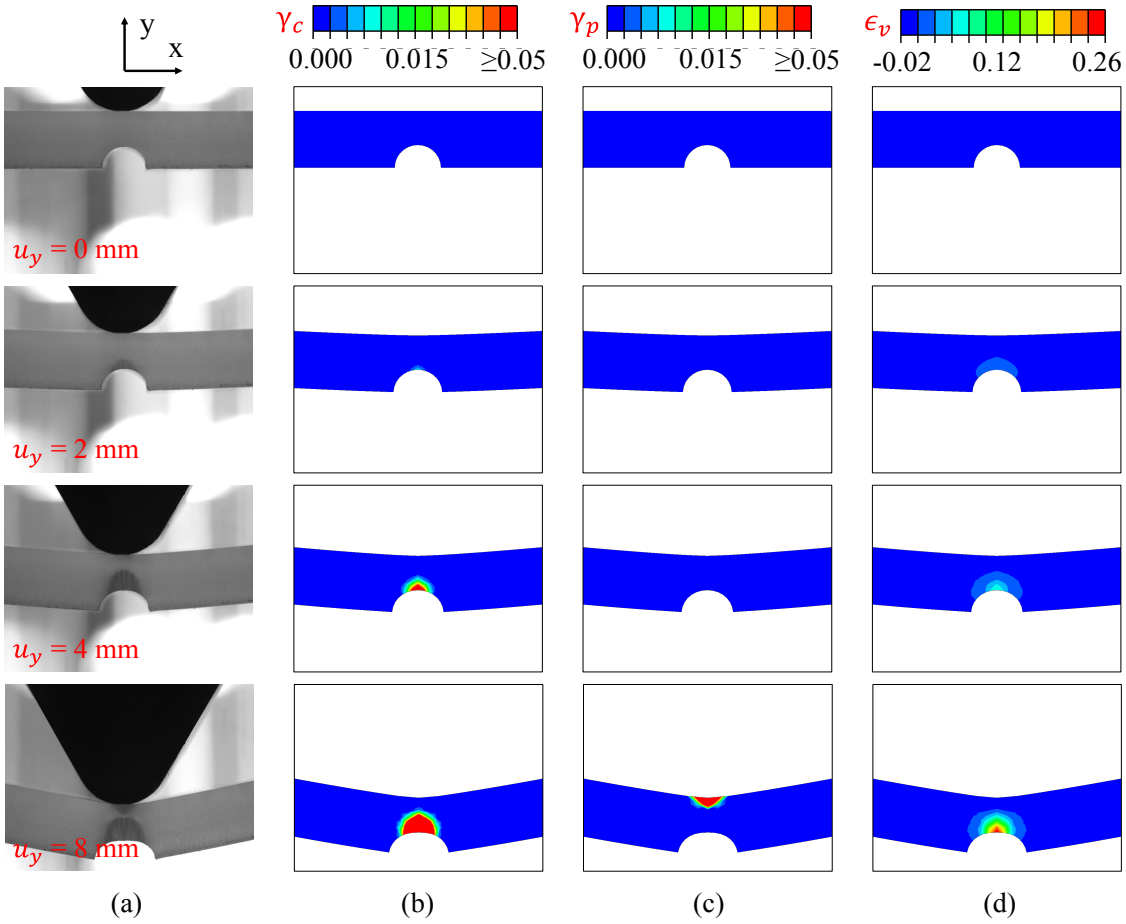

Figure 11: (a) Photographs of the notched bending test at different values of the applied displacement u_y. FE simulation predictions of the (b) accumulated crazing strain γ_c , (c) accumulated shear plastic strain γ_p, and (d) true volumetric strain ε_v at the same loading stages. Regions with γ_c and γ_p greater than 0.05 are shown in red in the contours.

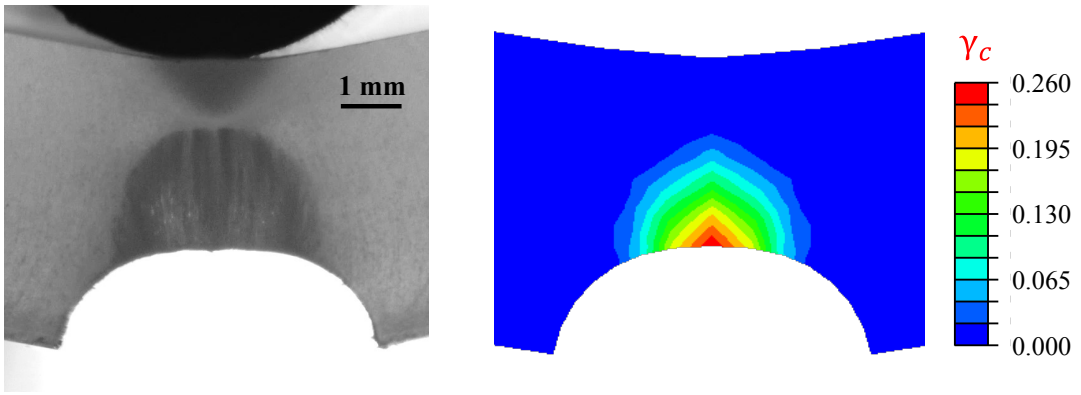

Figure 12: (a) Photograph of the root region of the notched bending test at $u_y = 8$ mm. (b) FE simulation of the accumulated crazing strain γ_c at $u_y = 8$ mm. Full scale is used in the contour of γ_c.

7. Application to PLA 3051D

In this section we apply our model to another grade of PLA (Ingeo 3051D, Natureworks), which was considered by Mirkhalaf and Fagerström (2021). We make the assumption that the tensile response of this grade of PLA is also dominated by craze yielding, based on the following considerations.

Although PLA 3051D is generally semicrystalline, its nucleation and crystallization rates are very slow, resulting in a very low crystallinity for the neat PLA sample (Richards et al., 2008; Fortunati et al., 2012). For instance, Richards et al. (2008) found that a fully amorphous state could be achieved through normal quenching. The degree of crystallinity 0.6% was also reported for the PLA 3051D measured by Differential Scanning Calorimeter (DSC) at the second heating after cooling at cooling rate of 10 °C/min (Fortunati et al., 2012). The PLA 3051D considered by Mirkhalaf and Fagerström (2021) was fabricated by hot-pressing followed by water cooling. In addition, the specimen was reported to be transparent (Mirkhalaf and Fagerström, 2021). Finally, the reported glass transition temperature for this grade is also very close to the purely amorphous PLA considered in the previous section, in the range 55 to 58 °C depending on the testing condition (Richards et al., 2008; Fortunati et al., 2012). Finally, the tensile stress-strain curves shown below are qualitatively very similar to those obtained with the previous grade. Based on these considerations, it is probable that the deformation mechansims of PLA 3051D and PLA4060D are similar.

Mirkhalaf and Fagerström (2021) carried out tensile tests on dog-bone specimens under cross-head velocities of 5, 10, and 16.8 mm min^{-1}, corresponding to engineering strain rates of 3×10^{-3}, 6×10^{-3}, and 1×10^{-2} s^{-1} in the gauge area at room temperature. They then employed the Eindhoven Glassy Polymer (EGP) model (Govaert et al., 2000), which assumes shear plasticity, for reproducing the experimental stress-strain curves. While the EGP could effectively replicate the experimental results, we believe that the deformation mechanisms in fact involved craze yielding, rather than shear plasticity. This assertion is based on the considerations listed above, along with the absence of necking reported by the authors and the observation that the dog-bone broke at a relatively small deformation, which is uncommon in a shear plasticity-dominated scenario.

We simulated the tensile test in a manner similar to Section 6.2. The geometry of the dog-bone specimen was the same as in the experiment, with front view shown in Fig. 13a

and a thickness of 0.1 mm. No geometric imperfection was used in this case. The geometry was discretised using 840 C3D8 elements. The material parameters were determined in a similar way to the previous section. Specifically, the modulus was determined from the slope of the stress-strain curve of 5 mm min^{-1}, and the Poisson's ratio was set to 0.35 based on results of the previous section. The crazing flow parameter $\frac{\Delta G_c}{k_B T}$ was identified from the strain-rate dependency of the yield stress. Remaining parameters were fitted on the experimental data of 5 mm min^{-1}. The same parameters are then used for predicting the experimental results of the other loading speeds. Numerical values of all parameters are collected in Table 2. The corresponding nominal stress and strain for the gauge region were calculated as: F/A_0 and u/L_0, where F is the force, A_0 is the initial cross-section area, u and L_0 are the cross-head displacement and initial gauge length, respectively. As shown in Fig. 13b, model predictions are in very good agreement with the experimental data at all the considered loading rates.

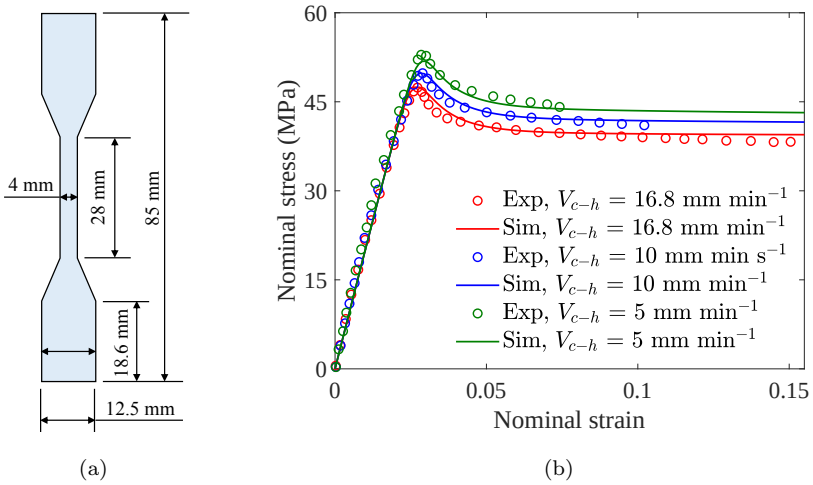

Figure 13: Comparison between model predictions and experimental results reported by Mirkhalaf and Fagerström (2021) for PLA 3051D. (a) Geometry of the specimen. (b) Nominal stress-strain curves for different cross-head velocities.

Table 2: Material parameters for PLA 3051D

Parameter	Unit	Value	Physical significance
$G^{(1)}$	MPa	1040	Shear modulus
$\lambda^{(1)}$	MPa	2420	Lamé's first parameter
$G_c^{(2)}$	MPa	18	Shear modulus of hardening branch for craze yielding
$\lambda_c^{(2)}$	MPa	0.18	Lamé's first parameter of hardening branch for craze yielding
h_c	-	300	Softening parameter relating to the softening slope for craze yielding
H_c^s	-	3.2	Softening parameter relating to the steady yield strength for craze yielding
$\dot{\gamma}_c^r$	s^{-1}	1	Reference flow rate for craze yielding
$\frac{\Delta G_c}{k_B T}$	-	19.8	Normalised activation energy for craze yielding
$\frac{V_c}{k_B T}$	MPa^{-1}	0.286	Normalised activation volume for craze yielding

8. Application to High-Impact Polystyrene (HIPS)

Although crazing often acts as a failure precursor in homogeneous polymers under tension, it plays an essential role in contributing to the high toughness of rubber-toughened thermoplastic polymers (Van der Giessen and Seelig, 2015; Helbig et al., 2016). This occurs because a large number of distributed crazes initiate within the plastic matrix between the scattered micro rubber particles during loading, leading to the dissipation of a substantial amount of energy. Collectively, these crazes can induce significant inelastic deformations before final failure. One of the most notable instances of this phenomenon is found in high-impact polystyrene (HIPS), where crazing is the main mechanism mediating inelastic deformations (Donald and Kramer, 1982; Bucknall, 2001). In this section, we illustrate the capability of our model in predicting the tensile response of HIPS under the assumption that inelastic deformation in tension is due to crazing. It should be noted that, in general, cavitation may also contribute to the inelastic deformation of rubber-toughened polymers (Yang and Liu, 2001; Bucknall, 2001). The development of a more comprehensive constitutive model describing inelastic deformations due to shear yielding, craze yielding and cavitation is left as future work.

We consider the experimental data for HIPS under tension reported by G'sell et al. (2002). The experiments were carried out on rectangular plates with overall dimensions of $63 \times 12 \times 4$ mm^3. A geometric defect was machined at the middle of the specimen, consisting in a reduction in width of the plate in a rounded profile extending over a length of 10 mm, as shown in Fig. 14. The minimum cross-section was a rectangle of 9.7×4.1 mm^2. The geometric defect caused the deformation to localise, and a video-controlled testing system was used to maintain constant axial true strain rate of 5×10^{-4} s^{-1} in the

minimum cross-section region. The intrinsic true tensile stress-strain and true volumetric strain-axial strain curves reported by G'sell et al. (2002) are shown in Fig. 14. Based on the intense dilatation process observed after the yield point (Fig. 14b), the authors concluded that the inelastic deformation of HIPS is governed by damage mechanisms (crazing, cavitation, decohesion, etc), rather than shear plasticity. Here we reproduced the experimental observations using our model for craze yielding at a single material point, assuming homogeneous uniaxial deformation in the strain localisation region. The material parameters collected in Table 3 were obtained by fitting the true stress-strain curve under the same strain rate. True stress-strain curves and true volumetric strain-axial strain curves predicted by the model are compared to experimental data in Fig. 14a and b, respectively. The model effectively replicates both sets of observations, which supports the hypothesis that crazing plays a significant role.

In another experiment, G'sell et al. (2002) considered the tension of a rectangular plate of the same HIPS with overall dimensions of $40.0 \times 8.0 \times 4.1$ mm^3 and containing a geometric defect so that the cross-section was reduced by 3.5% over a length of 10.0 mm at the centre of the specimen, see the inset in Fig. 15a. Experiments were conducted at a constant cross-head velocity of 2 mm min^{-1}. In the simulations, we discretised the geometry using 3500 C3D8 elements, and the boundary and loading conditions were set in a manner similar to the previous sections for dog-bone tensile tests. Material parameters were kept identical to the previous HIPS example.

Fig. 15a shows the comparison between the nominal stress-strain curves obtained with the model and measured experimentally. Here, the nominal stress is defined as the force F divided by the initial area of the cross-section A_0, and the nominal strain ϵ is defined as $\epsilon = (L - L_0)/L_0$, where L and L_0 are the initial and current distances between the two cross-heads, respectively. Again, the overall behaviour is well captured and the accuracy is acceptable, although there is some discrepancy in the elastic region, which can be explained as follows. First, small variations in material properties between the two specimens may exist; second, the experimental setup inevitably introduced some systematic errors, since the true strain at the point of interest was calculated by non-linear interpolation from the surrounding points and the markers used for tracing the deformation at a location was deformed. This was also recognized by the authors of the reference (G'sell et al., 2002) from which we extracted the data. Lastly, viscoelasticity was

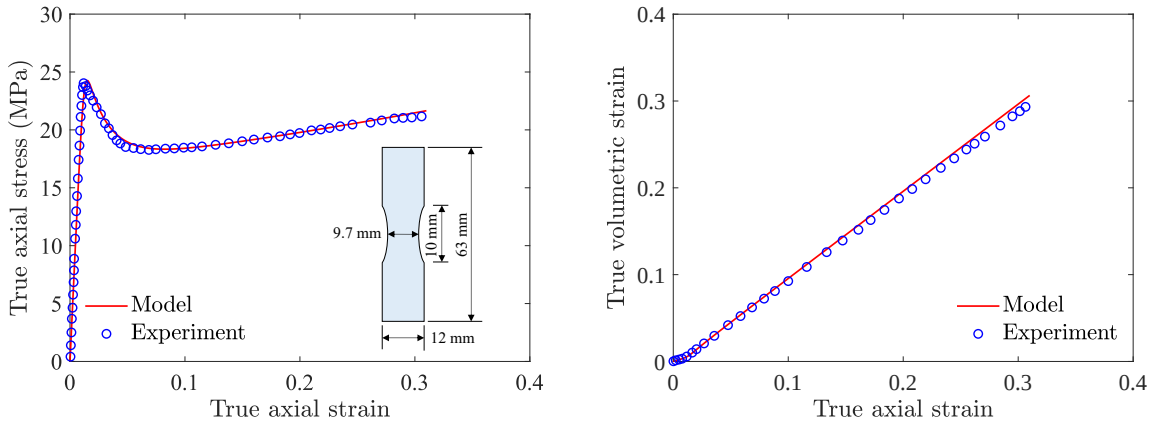

(a) (b)

Figure 14: Comparison between model predictions and experimental results reported by G'sell et al. (2002) for HIPS in a tensile test at a constant true rate of 5×10^{-4} s^{-1}. (a) True stress-strain curve. (b) True volumetric strain vs. true axial strain curve. The geometry of the specimen is shown in the inset of Fig (a).

Table 3: Material parameters for HIPS

Parameter	Unit	Value	Physical significance
$G^{(1)}$	MPa	808	Shear modulus
$\lambda^{(1)}$	MPa	1212	Lamé's first parameter
$G_c^{(2)}$	MPa	14.5	Shear modulus of hardening branch for craze yielding
$\lambda_c^{(2)}$	MPa	0.145	Lamé's first parameter of hardening branch for craze yielding
h_c	-	100	Softening parameter relating to the softening slope for craze yielding
H_c^s	-	2.2	Softening parameter relating to the steady yield strength for craze yielding
$\dot{\gamma}_c^r$	s^{-1}	1	Reference flow rate for craze yielding
$\frac{\Delta G_c}{k_B T}$	-	13.5	Normalised activation energy for craze yielding
$\frac{V_c}{k_B T}$	MPa^{-1}	0.26	Normalised activation volume for craze yielding

neglected in the model, which could perhaps play a role on the accuracy of the prediction. The simulation also shows that no necking appears during the deformation process, which is consistent with the experimental observations, see Fig. 15b.

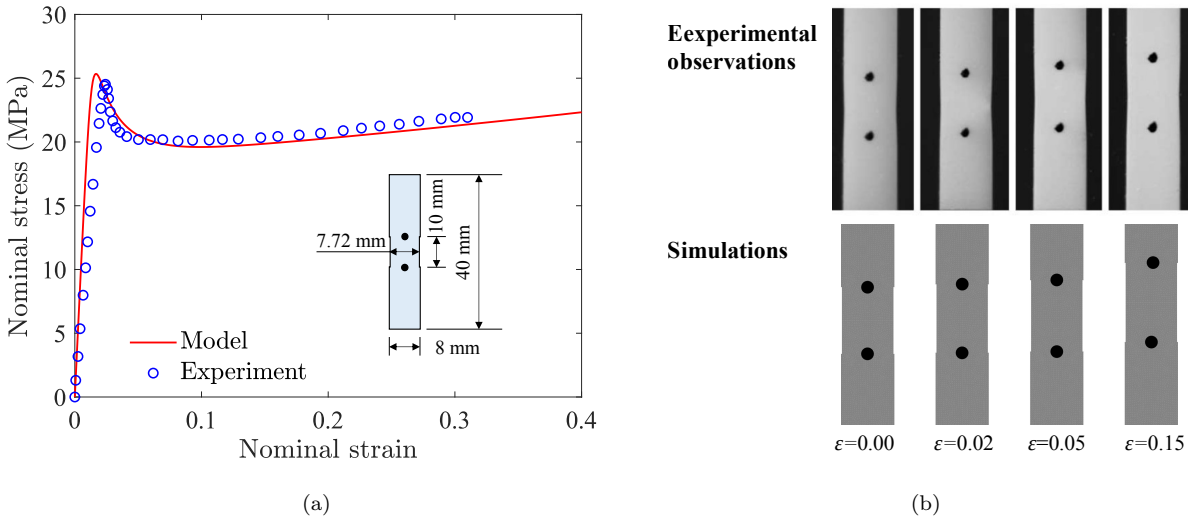

(a) (b)

Figure 15: Comparison between model predictions and experimental results reported by G'sell et al. (2002) for a parallelepipedic HIPS specimen with a geometric defect in the middle and subjected to a constant cross-head velocity of 2 mm min^{-1}. (a) Nominal stress-strain curve. (b) Illustration of the deformed shape. The geometry of the specimen is shown in the inset of Fig (a).

9. Conclusions

In this study, we have proposed a thermodynamically consistent constitutive model for glassy polymers that considers shear plasticity and craze yielding. We regard craze yielding as a continuous viscoplastic deformation process at the macroscale, which can be modelled in a manner similar to conventional finite viscoplasticity, with the main difference lying in the driving force and flow rule. The key difference between shear plasticity and craze yielding is that shear plasticity is a volume-preserving deformation mechanism while craze yielding induces a significant volume increase. A stress-based switching rule for selecting the inelastic deformation mechanism was introduced. The proposed model was implemented in Abaqus via a user-subroutine UMAT.

We have compared model predictions and our experimental data for PLA under different loading conditions, including compression, tension, bending, and notched bending. This set of experimental results could be valuable for researchers for the development and validation of improved models. Additionally, comparison between model simulations and experimental data from literature for another grade of PLA and HIPS, where craze yielding is also believed to be the dominant mechanism, was also performed.

The extensive comparison studies demonstrate that our model can reproduce experimental observations very well. Specifically, the advantages of our model and the main

findings can be summarised as follows: (1) our model can account for yielding, softening, and flowing under both shear plasticity and craze yielding; (2) our model provides accurate predictions of volumetric strain for PLA and HIPS; (3) our model can predict strain localisation without necking in tensile tests, which follows from the dilatational nature of crazing; (4) our model produces reasonable predictions in complex scenarios where both mechanisms simultaneously occur at different locations of the specimen.

In future work, the thermodynamic framework could be improved by considering thermo-mechanical coupling to get more accurate predictions under moderate to large strain rates where adiabatic heating plays a role. Other forms of the specific constitutive equations for softening and rehardening could also be considered to improve the predictions. Additionally, the framework could also be generalised to describe the effect of other dilatant mechanisms, such as cavitation, and to include a macroscopic failure criterion.

Acknowledgements

This work was supported by a Future Leaders Fellowship of UK Research and Innovation [MR/W006995/1]. The authors also acknowledge additional support of EPSRC under Award EP/V003321/1.

Appendix A. DIC parameters

Table A1: DIC parameters

Parameters	Unit	Value
Image filtering	-	Gaussian
Interpolation	-	Local bicubic spline interpolation
Strain interpolation	-	Bilinear quadrilateral
Subset shape function	-	Affine
Average speckle size	pixels	5
Subset size	pixels	31
Step size	pixels	7
Length scale	mm/pixel	0.0214
Strain window size	points	5
Virtual strain gauge size	pixels	59

Appendix B. Numerical algorithm and implementation

Appendix B.1. Integration procedure of the evolution equations

Taking $H_p(0) = 0$, Eq. (32) can be integrated analytically as:

$$H_p = H_p^s \left[1 - \exp\left(\frac{-h_p \gamma_p}{H_p^s}\right)\right] \tag{B.1}$$

where γ_p is the accumulated plastic strain: $\gamma_p = \int_0^t \dot{\gamma}_p dt'$.

We carried out the integration of Eq. (29) over a time interval $[t_n, t_{n+1}]$ using a predictor-corrector two-step algorithm. In the elastic predictor step, the inelastic strain is assumed fixed to its value at the previous time step. The trial elastic left Cauchy-Green tensor is given by:

$$(\boldsymbol{b}_e)_{tr} = \boldsymbol{F}_{n+1} (\boldsymbol{C}_i^{-1})_n \boldsymbol{F}_{n+1}^T \tag{B.2}$$

In the plastic corrector step, the total deformation is held fixed, which leads to $\mathcal{L}_v \boldsymbol{b}_e = \dot{\boldsymbol{b}}_e$. q. (29) then provides:

$$\dot{\boldsymbol{b}}_e = -\left(2\dot{\gamma}_p \boldsymbol{N}_p\right) \boldsymbol{b}_e \tag{B.3}$$

Solving the above equation using the exponential mapping technique (Doghri, 2000) gives

$$\boldsymbol{b}_e = \exp\left[-2 \int_{t_n}^{t_{n+1}} \left(\dot{\gamma}_p \boldsymbol{N}_p\right) dt\right] (\boldsymbol{b}_e)_{tr} \tag{B.4}$$

Using a first-order approximation of the integration in Eq. (B.4), we have

$$\boldsymbol{b}_e \approx \exp\left[-2\Delta t \left(\dot{\gamma}_p \boldsymbol{N}_p\right)_{n+1}\right] (\boldsymbol{b}_e)_{tr} \tag{B.5}$$

For convenience, in what follows, we will drop the subscript $n+1$. Eq. (B.5) can be rewritten as

$$(\boldsymbol{b}_e)_{tr} \approx \exp\left[2\Delta t\,(\dot{\gamma}_p \boldsymbol{N}_p)\right] \boldsymbol{b}_e \tag{B.6}$$

The spectral decomposition of $(\boldsymbol{b}_e)_{tr}$ can be written as:

$$(\boldsymbol{b}_e)_{tr} = \sum_{A=1}^{3} (\lambda_{e,A})_{tr}^2\, (\boldsymbol{n}_A)_{tr} \otimes (\boldsymbol{n}_A)_{tr} \tag{B.7}$$

where $(\lambda_{e,A})_{tr}$ and $(\boldsymbol{n}_A)_{tr}$ are the eigenvalues and eigenvectors of $(\boldsymbol{b}_e)_{tr}$.

Similarly, the spectral decomposition of $\boldsymbol{b}_e$ can be expressed as:

$$\boldsymbol{b}_e = \sum_{A=1}^{3} (\lambda_{e,A})^2\, \boldsymbol{n}_A \otimes \boldsymbol{n}_A \tag{B.8}$$

where $\lambda_{e,A}$ and $(\boldsymbol{n}_A)$ are the eigenvalues and eigenvectors of $\boldsymbol{b}_e$.

For isotropic materials, $\boldsymbol{\tau}^{(1)}$ commutes with $\boldsymbol{N}_p$ and $\boldsymbol{b}_e$, therefore, $\boldsymbol{N}_p$ and $\boldsymbol{b}_e$ also commute with each other. Then Eq. (B.6) can be rewritten as (Doghri, 2000):

$$(\boldsymbol{b}_e)_{tr} \approx \sum_{A=1}^{3} \exp\left[2\Delta t\,(\dot{\gamma}_p N_{p,A})\right] (\lambda_{e,A})^2\, \boldsymbol{n}_A \otimes \boldsymbol{n}_A \tag{B.9}$$

Comparing Eqs. (B.7) and (B.9), from the uniqueness of the spectral decomposition, we conclude that $\boldsymbol{b}_e$ also commutes with $(\boldsymbol{b}_e)_{tr}$ and that

$$\lambda_{e,A}^2 = (\lambda_{e,A}^2)_{tr} \exp(-2\Delta t(\dot{\gamma}_p N_{p,A})) \tag{B.10}$$

Taking the logarithm on both sides, we have

$$\epsilon_{e,A} = (\epsilon_{e,A})_{tr} - \Delta t \dot{\gamma}_p N_{p,A} \tag{B.11}$$

where $E_{e,A} = \ln(\lambda_{e,A}), (E_{e,1})_{tr} = \ln((\lambda_{e,A})_{tr})$.

Eq. (B.11) constitutes a system of nonlinear equations which can be solved using the Newton-Raphson method. However, after some manipulations, the system of equations can be reduced to one scalar equation for one scalar unknown $\dot{\gamma}_p$, which greatly simplifies the problem. Taking the deviatoric part of Eq. (B.11) and multiplying by $2G^{(1)}$, we obtain:

$$\tilde{\tau_A}^{(1)} = (\tilde{\tau_A}^{(1)})_{tr} - 2G^{(1)}\Delta t\dot{\gamma}_p \frac{\tilde{\tau_A}^{(1)}}{\sqrt{2}\tau^{(1)}} \tag{B.12}$$

Rearrange the above equation, we have

$$\tilde{\tau_A}^{(1)} = \left(1 - \frac{\sqrt{2}G^{(1)}\Delta t\dot{\gamma}_p}{(\tau^{(1)})_{tr}}\right) (\tilde{\tau_A}^{(1)})_{tr} \tag{B.13}$$

Then combining Eqs. (31) and (B.13), the simplified scalar equation for $\dot{\gamma}_p$ is obtained as:

$$r_p = \frac{k_B T}{V_p} \arcsin\left[\frac{\dot{\gamma}_p}{\dot{\gamma}_p^r \exp\left(-\Delta G_p / k_B T + H_p\right)}\right] - (\tau^{(1)})_{tr} + \sqrt{2} G^{(1)} \Delta t \dot{\gamma}_p \tag{B.14}$$

In a similar way, for craze yielding, a single scalar equation for $\dot{\gamma}^c$ is obtained as:

$$r_c = \frac{k_B T}{V_c} \arcsin\left[\frac{\dot{\gamma}_c}{\dot{\gamma}_c^r \exp\left(-\Delta G_c / k_B T + H_c\right)}\right] - (\tau_1^{(1)})_{tr} + \left(2G^{(1)} + \lambda^{(1)}\right) \Delta t \dot{\gamma}_c \tag{B.15}$$

The tangents for Eqs. (B.14) and (B.15) are respectively given by

$$\frac{\partial r_p}{\partial \dot{\gamma}_p} = \frac{k_B T}{V_p} \frac{1}{\sqrt{C_2^2 + 1}} \frac{\partial C_2}{\partial \dot{\gamma}_p} + \sqrt{2} G^{(1)} \Delta t \tag{B.16}$$

where

$$\begin{aligned}
C_2 &= \frac{\dot{\gamma}_p}{C_1} \\
C_1 &= \dot{\gamma}_p^r \exp\left(-\frac{\Delta G_p}{k_B T} + H_p\right) \\
\frac{\partial C_2}{\partial \dot{\gamma}_p} &= \frac{1 - \dot{\gamma}_p \frac{\partial H_p}{\partial \dot{\gamma}_p}}{C_1} \\
\frac{\partial H_p}{\partial \dot{\gamma}_p} &= h_p \Delta t \exp\left(-\frac{h_p \bar{\gamma}_p}{H_p^s}\right)
\end{aligned}$$

and

$$\frac{\partial r_c}{\partial \dot{\gamma}_c} = \frac{k_B T}{V_c} \frac{1}{\sqrt{C_4^2 + 1}} \frac{\partial C_4}{\partial \dot{\gamma}_c} + \left(2G^{(1)} + \lambda^{(1)}\right) \Delta t \tag{B.17}$$

where

$$\begin{aligned}
C_4 &= \frac{\dot{\gamma}_c}{C_3} \\
C_3 &= \dot{\gamma}_c^r \exp\left(-\frac{\Delta G_c}{k_B T} + H_c\right) \\
\frac{\partial C_4}{\partial \dot{\gamma}^c} &= \frac{1 - \dot{\gamma}_c \frac{\partial H_c}{\partial \dot{\gamma}_c}}{C_3} \\
\frac{\partial H_c}{\partial \dot{\gamma}_c} &= h_c \Delta t \exp\left(-\frac{h_c \bar{\gamma}_c}{H_c^s}\right)
\end{aligned}$$

Appendix B.2. Consistent tangent moduli

The consistent jacobian moduli (or DDSDDE in Abaqus) based on the Jaumman rate, an objective rate form, of the Kirchoff stress tensor, $\overset{\nabla}{\boldsymbol{\tau}}$, can be derived through (Smith, 2009; Nguyen and Waas, 2016):

$$\overset{\nabla}{\boldsymbol{\tau}} = \mathbb{c} : \boldsymbol{d} + \boldsymbol{d}\boldsymbol{\tau} + \boldsymbol{\tau}\boldsymbol{d} \tag{B.18}$$

where the rate of deformation tensor $\boldsymbol{d}$ is defined as $\boldsymbol{d} = \frac{1}{2}(\boldsymbol{l} + \boldsymbol{l}^T)$ in which $\boldsymbol{l} = \dot{\boldsymbol{F}}\boldsymbol{F}^{-1}$ is the spatial velocity gradient, $\mathbb{c}$ is the elasticity tensor in the spatial description given by:

$$\mathbb{c}_{ijkl} = F_{iI}F_{jJ}F_{kK}F_{lL}\frac{\partial S_{IJ}}{\partial E_{KL}} = \mathbb{c}^{(1)}_{ijkl} + \mathbb{c}^{(2)}_{ijkl} \tag{B.19}$$

where

$$\mathbb{c}^{(1)}_{ijkl} = F_{iI}F_{jJ}F_{kK}F_{lL}\frac{\partial S^{(1)}_{IJ}}{\partial E_{KL}}, \quad \mathbb{c}^{(2)}_{ijkl} = F_{iI}F_{jJ}F_{kK}F_{lL}\frac{\partial S^{(2)}_{IJ}}{\partial E_{KL}} \tag{B.20}$$

with $E_{IJ} = \frac{1}{2}(F_{kI}F_{kJ} - \delta_{IJ})$ is the Green-Lagrange strain tensor. Eq. (B.19) shows that the elasticity tensor in the spatial description $\mathbb{c}_{ijkl}$ can be calculated by pushing forward of the elasticity tensor in the material description $\frac{\partial S_{IJ}}{\partial E_{KL}}$.

In Abaqus,

$$\overset{\nabla}{\boldsymbol{\tau}} = J(\text{DDSDDE}) : \boldsymbol{d} \tag{B.21}$$

Therefore,

$$(\text{DDSDDE})_{ijkl} = \frac{1}{J}\left(\mathbb{c}^{(1)}_{ijkl} + \mathbb{c}^{(2)}_{ijkl}\right) + \frac{1}{2}\left(\sigma_{ij}\delta_{kl} + \sigma_{kl}\delta_{ij} + \sigma_{il}\delta_{jk} + \sigma_{jk}\delta_{il}\right) \tag{B.22}$$

However, instead of calculating $\mathbb{c}^{(1)}$ using Eq. (B.20) like (Bonet et al., 2016), an alternative method is proposed by Reese and Govindjee (1998). The second Piola-Kirchoff stress tensor in the non-equilibrium can be rewritten as (Reese and Govindjee, 1998):

$$\boldsymbol{S}^{(1)} = \boldsymbol{F}^{-1}\boldsymbol{\tau}^{(1)}\boldsymbol{F}^{-1} = (\boldsymbol{F}_i^{-1})_{n-1}\underbrace{(\boldsymbol{F}_e^{-1})_{tr}\boldsymbol{\tau}^{(1)}(\boldsymbol{F}_e^{T})_{tr}}_{\tilde{\boldsymbol{S}}^{(1)}}(\boldsymbol{F}_i^{-T})_{n-1} \tag{B.23}$$

Then, the elasticity tensor $\mathbb{c}^{(1)}_{ijkl}$ can be further expressed as:

$$\mathbb{c}^{(1)}_{ijkl} = (F_{e,iI})_{tr}(F_{e,jJ})_{tr}(F_{e,kK})_{tr}(F_{e,lL})_{tr}\frac{\partial(\tilde{S}^{(1)}_{IJ})}{\partial(E_{e,KL})_{tr}} \tag{B.24}$$

Introduce the spectral decomposition

$$\tilde{\boldsymbol{S}}^{(1)} = \sum_{i=1}^{3}\frac{\tau^{(1)}_i}{(\lambda^2_{e,i})_{tr}}\tilde{\boldsymbol{N}}_i \otimes \tilde{\boldsymbol{N}}_i \tag{B.25}$$

We then have

$$\begin{aligned}\tilde{\mathbb{c}}_{ijkl} = \frac{\partial(\tilde{S}^{(1)}_{ij})}{\partial(E_{e,kl})_{tr}} &= \sum_{i=1}^{3}\sum_{j=1}^{3} L_{ij}\tilde{\boldsymbol{N}}_i \otimes \tilde{\boldsymbol{N}}_i \otimes \tilde{\boldsymbol{N}}_j \otimes \tilde{\boldsymbol{N}}_j \\ &+ \sum_{i=1}^{3}\sum_{\substack{j=1\\ j\neq i}}^{3} G_{ij}\left(\tilde{\boldsymbol{N}}_i \otimes \tilde{\boldsymbol{N}}_j \otimes \tilde{\boldsymbol{N}}_i \otimes \tilde{\boldsymbol{N}}_j + \tilde{\boldsymbol{N}}_i \otimes \tilde{\boldsymbol{N}}_j \otimes \tilde{\boldsymbol{N}}_j \otimes \tilde{\boldsymbol{N}}_i\right) \\ &= \sum_{i=1}^{3}\sum_{j=1}^{3}\sum_{k=1}^{3}\sum_{l=1}^{3}\tilde{L}_{ijkl}\tilde{\boldsymbol{N}}_i \otimes \tilde{\boldsymbol{N}}_j \otimes \tilde{\boldsymbol{N}}_k \otimes \tilde{\boldsymbol{N}}_l\end{aligned} \tag{B.26}$$

where

$$L_{ij} = \frac{T_{ij} - 2\tau_i^{(1)}\delta_{ij}}{(\lambda_{e,i}^2)_{tr}(\lambda_{e,j}^2)_{tr}} \quad i,j = 1,2,3 \tag{B.27}$$

$$G_{ij} = \begin{cases} \frac{S_j^{(1)} - S_i^{(1)}}{(\lambda_{e,i}^2)_{tr} - (\lambda_{e,j}^2)_{tr}}, & \text{if } (\lambda_{e,i})_{tr} \neq (\lambda_{e,j})_{tr} \\ \frac{1}{2}\left(L_{ii} - L_{jj}\right) & \text{if } (\lambda_{e,i})_{tr} = (\lambda_{e,j})_{tr} \end{cases} \tag{B.28}$$

where

$$T_{ij} = \frac{\partial \tau_i^{(1)}}{\partial (\epsilon_{e,j})_{tr}} = \frac{\partial \tilde{\tau}_i^{(1)}}{\partial (\epsilon_{e,j})_{tr}} + \frac{\partial p}{\partial (\epsilon_{e,j})_{tr}} \tag{B.29}$$

where $p = \frac{1}{3}\mathrm{tr}(\boldsymbol{\tau})$ is the hydrostatic stress.

According to Eq. (B.13), we have

$$\begin{aligned} \frac{\partial \tilde{\tau}_i^{(1)}}{\partial (\epsilon_{e,j})_{tr}} = & \left(1 - \frac{\sqrt{2}G^{(1)}\Delta t\dot{\gamma}_p}{(\tau^{(1)})_{tr}}\right) \frac{\partial (\tilde{\tau}_i^{(1)})_{tr}}{\partial (\epsilon_{e,j})_{tr}} \\ & + \frac{\sqrt{2}G^{(1)}\Delta t(\tilde{\tau}_i^{(1)})_{tr}}{(\tau^{(1)})_{tr}^2}\left(\frac{(\tau^{(1)})_{tr}}{C_3 + \sqrt{2}G^{(1)}\Delta t} - \dot{\gamma}_p\right) \frac{\partial (\tau^{(1)})_{tr}}{\partial (\epsilon_{e,j})_{tr}} \end{aligned} \tag{B.30}$$

$$\frac{\partial (\tilde{\tau}_i^{(1)})_{tr}}{\partial (\epsilon_{e,j})_{tr}} = 2G^{(1)}\delta_{ij} - \frac{2}{3}G^{(1)}, \quad \frac{\partial p}{\partial (\epsilon_{e,j})_{tr}} = \lambda^{(1)}, \quad \frac{\partial (\tau^{(1)})_{tr}}{\partial (\epsilon_{e,j})_{tr}} = \frac{1}{2(\tau^{(1)})_{tr}} \sum_{i=1}^{3} (\tilde{\tau}_i^{(1)})_{tr} \frac{\partial (\tilde{\tau}_i^{(1)})_{tr}}{\partial (\epsilon_{e,j})_{tr}} \tag{B.31}$$

Finally, $\mathbb{c}_{ijkl}$ can be derived by pushing forward $\tilde{\mathbb{c}}_{ijkl}$ with $(\boldsymbol{F}_e)_{tr}$:

$$\mathbb{c}_{ijkl} = \sum_{i=1}^{3}\sum_{j=1}^{3}\sum_{k=1}^{3}\sum_{l=1}^{3} \tilde{L}_{ijkl}(\lambda_{e,i})_{tr}(\lambda_{e,j})_{tr}(\lambda_{e,k})_{tr}(\lambda_{e,l})_{tr}\boldsymbol{n}_i \otimes \boldsymbol{n}_j \otimes \boldsymbol{n}_k \otimes \boldsymbol{n}_l \tag{B.32}$$

For craze yielding, the stiffness tensor has the same form as Eq. (B.32). The only difference lies in that the expression of T_{ij} for craze yielding is expressed as:

$$T_{ij} = \frac{\partial \tau_i^{(1)}}{\partial (\epsilon_{e,j})_{tr}} = \frac{\partial \tau_i^{(1)}}{\partial \epsilon_K} \frac{\partial \epsilon_K}{\partial (\epsilon_{e,j})_{tr}} \tag{B.33}$$

where

$$\frac{\partial \tau_i^{(1)}}{\partial \epsilon_K} = 2G^{(1)}\delta_{iK} + \lambda^{(1)} \tag{B.34}$$

$$\frac{\partial \epsilon_K}{\partial (\epsilon_j)_{tr}} = \begin{cases} 1, & \text{if } j \neq 1 \\ 1 - \Delta t \frac{\partial \dot{\gamma}_c}{\partial \epsilon_{e,j}}, & \text{if } j = 1 \end{cases} \tag{B.35}$$

where

$$\frac{\partial \dot{\gamma}_c}{\partial \epsilon_j} = \frac{2G^{(1)} + \lambda^{(1)}}{C_4 + \left(2G^{(1)} + \lambda^{(1)}\right)\Delta t} \tag{B.36}$$

In the hardening branch for both shear plasticity and craze yielding, it is easy to show that

$$\mathbb{c}_{ijkl}^{(2)} = \left(G^{(2)} - \lambda^{(2)}\ln J\right)\left(\delta_{il}\delta_{jk} + \delta_{ik}\delta_{jl}\right) + \lambda_{eq}\delta_{ij}\delta_{kl} \tag{B.37}$$

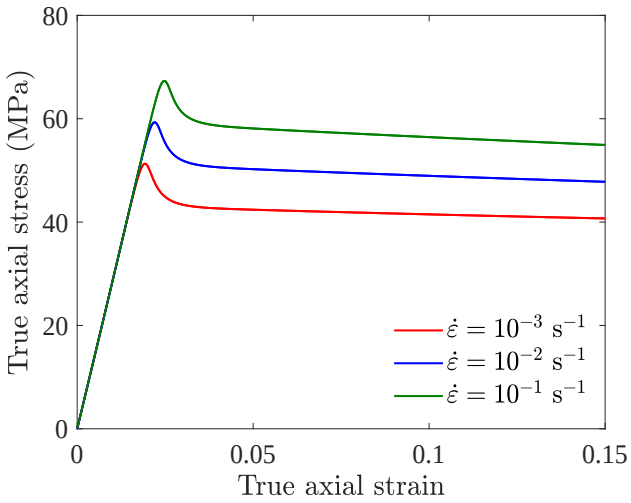

Figure C.16: True stress-strain curves in tension for PLA 4060D under different strain rates at 37 °C.

Appendix C. True tensile response of PLA 4060D

The true stress-strain curves in tension for PLA 4060D under the same true strain rates as in our compression tests are shown in Fig. C.16.

References

Alves, A.F.C., Ferreira, B.P., Pires, F.A., 2023. A constitutive model for amorphous thermoplastics from low to high strain rates: Formulation and computational aspects. International Journal of Plasticity 169, 103712.

Anand, L., 1985. Constitutive equations for hot-working of metals. International Journal of Plasticity 1, 213–231.

Anand, L., Ames, N.M., Srivastava, V., Chester, S.A., 2009. A thermo-mechanically coupled theory for large deformations of amorphous polymers. Part I: formulation. International Journal of Plasticity 25, 1474–1494.

Anand, L., Aslan, O., Chester, S.A., 2012. A large-deformation gradient theory for elastic–plastic materials: strain softening and regularization of shear bands. International Journal of Plasticity 30, 116–143.

Argon, A., 1973a. A theory for the low-temperature plastic deformation of glassy polymers. Philosophical Magazine 28, 839–865.

Argon, A., 1979. Plastic deformation in metallic glasses. Acta metallurgica 27, 47–58.

Argon, A., 2011. Craze initiation in glassy polymers–revisited. Polymer 52, 2319–2327.

Argon, A.S., 1973b. Physical basis of distortional and dilational plastic flow in glassy polymers. Journal of Macromolecular Science, Part B 8, 573–596.

Argon, A.S., 2013. The physics of deformation and fracture of polymers. New York.: Cambridge .

Argon, A.S., Hannoosh, J.G., 1977. Initiation of crazes in polystyrene. Philosophical Magazine 36, 1195–1216.

Arruda, E.M., Boyce, M.C., 1993. Evolution of plastic anisotropy in amorphous polymers during finite straining. International Journal of Plasticity 9, 697–720.

Bazant, Z.P., Jirásek, M., 2002. Nonlocal integral formulations of plasticity and damage: survey of progress. Journal of Engineering Mechanics 128, 1119–1149.

Bergström, J.S., Boyce, M.C., 1998. Constitutive modeling of the large strain time-dependent behavior of elastomers. Journal of the Mechanics and Physics of Solids 46, 931–954.

Bonet, J., Gil, A., Wood, R., 2016. Nonlinear Solid Mechanics for Finite Element Analysis: Statics. Cambridge University Press.

Boyce, M.C., Parks, D.M., Argon, A.S., 1988. Large inelastic deformation of glassy polymers. Part I: rate dependent constitutive model. Mechanics of Materials 7, 15–33.

Buckley, C., Jones, D., 1995. Glass-rubber constitutive model for amorphous polymers near the glass transition. Polymer 36, 3301–3312.

Bucknall, C., 2001. Applications of microscopy to the deformation and fracture of rubber-toughened polymers. Journal of microscopy 201, 221–229.

Bucknall, C.B., 2007a. New criterion for craze initiation. Polymer 48, 1030–1041.

Bucknall, C.B., 2007b. New criterion for craze initiation. Polymer 48, 1030–1041.

Chen, H., Pan, Z., Yuan, D., Sulley, G.S., Oosterbeek, R.N., Williams, C.K., Brassart, L., 2023. Shear yielding and crazing in dry and wet amorphous PLA at body temperature. Polymer 289, 126477.

Chevalier, J., Brassart, L., Lani, F., Bailly, C., Pardoen, T., Morelle, X.P., 2018. Unveiling the nanoscale heterogeneity controlled deformation of thermosets. Journal of the Mechanics and Physics of Solids 121, 432–446.

Deblieck, R.A., Van Beek, D., Remerie, K., Ward, I.M., 2011. Failure mechanisms in polyolefines: The role of crazing, shear yielding and the entanglement network. Polymer 52, 2979–2990.

Doghri, I., 2000. Mechanics of deformable solids: linear, nonlinear, analytical and computational aspects. Springer Science & Business Media.

Donald, A.M., Kramer, E.J., 1982. Plastic deformation mechanisms in poly (acrylonitrile-butadiene styrene)[abs]. Journal of Materials Science 17, 1765–1772.

Estevez, R., Tijssens, M., Van der Giessen, E., 2000. Modeling of the competition between shear yielding and crazing in glassy polymers. Journal of the Mechanics and Physics of Solids 48, 2585–2617.

Eyring, H., 1936. Viscosity, plasticity, and diffusion as examples of absolute reaction rates. The Journal of Chemical Physics 4, 283–291.

Farah, S., Anderson, D.G., Langer, R., 2016. Physical and mechanical properties of pla, and their functions in widespread applications - a comprehensive review. Advanced Drug Delivery Reviews 107, 367–392.

Fortunati, E., Armentano, I., Zhou, Q., Puglia, D., Terenzi, A., Berglund, L.A., Kenny, J.M., 2012. Microstructure and nonisothermal cold crystallization of pla composites based on silver nanoparticles and nanocrystalline cellulose. Polymer degradation and stability 97, 2027–2036.

Gearing, B., Anand, L., 2004a. Notch-sensitive fracture of polycarbonate. International Journal of Solids and Structures 41, 827–845.

Gearing, B., Anand, L., 2004b. On modeling the deformation and fracture response of glassy polymers due to shear-yielding and crazing. International Journal of Solids and Structures 41, 3125–3150.

Gent, A.N., 1996. A new constitutive relation for rubber. Rubber chemistry and technology 69, 59–61.

Van der Giessen, E., Seelig, T., 2015. Computational modeling of rubber-toughening in amorphous thermoplastic polymers: a review. International Journal of Fracture 196, 207–222.

Govaert, L., Timmermans, P., Brekelmans, W., 2000. The influence of intrinsic strain softening on strain localization in polycarbonate: modeling and experimental validation. The Journal of Engineering Materials and Technology 122, 177–185.

G'sell, C., Hiver, J., Dahoun, A., 2002. Experimental characterization of deformation damage in solid polymers under tension, and its interrelation with necking. International Journal of Solids and Structures 39, 3857–3872.

Guo, S., Torres, D., Weygand, S., Olagnon, C., Estevez, R., 2015. 3d study of the competitions between shear yielding and crazing for a variable thickness on ductile polymers. Engineering Fracture Mechanics 149, 230–249.

Hasan, O., Boyce, M., 1995. A constitutive model for the nonlinear viscoelastic viscoplastic behavior of glassy polymers. Polymer Engineering & Science 35, 331–344.

Haward, R., Thackray, G.., 1968. The use of a mathematical model to describe isothermal stress-strain curves in glassy thermoplastics. Proceedings of the Royal Society of London. Series A. Mathematical and Physical Sciences 302, 453–472.

Haward, R.N., 1997. The physics of glassy polymers. Springer Science & Business Media.

Helbig, M., Van Der Giessen, E., Clausen, A.H., Seelig, T., 2016. Continuum-micromechanical modeling of distributed crazing in rubber-toughened polymers. European Journal of Mechanics-A/Solids 57, 108–120.

Hoare, J., Hull, D., 1972. Craze yielding and stress-strain characteristics of crazes in polystyrene. Philosophical Magazine 26, 443–455.

Horgan, C.O., Saccomandi, G., 2004. Constitutive models for compressible nonlinearly elastic materials with limiting chain extensibility. Journal of Elasticity 77, 123–138.

Huang, R., Zheng, S., Liu, Z., Ng, T.Y., 2020. Recent advances of the constitutive models of smart materials—hydrogels and shape memory polymers. International Journal of Applied Mechanics 12, 2050014.

Ishikawa, M., Narisawa, I., Ogawa, H., 1977. Criterion for craze nucleation in polycarbonate. Journal of Polymer Science: Polymer Physics Edition 15, 1791–1804.

Kramer, E.J., 1983. Microscopic and molecular fundamentals of crazing, in: Crazing in polymers. Springer, pp. 1–56.

Lai, J., Van der Giessen, E., 1997. A numerical study of crack-tip plasticity in glassy polymers. Mechanics of Materials 25, 183–197.

Lee, E.H., 1969. Elastic-Plastic Deformation at Finite Strains. Journal of Applied Mechanics 36, 1–6.

Lin, J., Qian, J., Xie, Y., Wang, J., Xiao, R., 2023. A mean-field shear transformation zone theory for amorphous polymers. International Journal of Plasticity 163, 103556.

Liu, F., Wang, J., Long, S., Zhang, H., Yao, X., 2022. Experimental and modeling study of the viscoelastic-viscoplastic deformation behavior of amorphous polymers over a wide temperature range. Mechanics of Materials 167, 104246.

MatchID, 2023. MatchID. https://www.matchid.eu/.

McCutcheon, C.J., Zhao, B., Jin, K., Bates, F.S., Ellison, C.J., 2020. Crazing mechanism and physical aging of poly (lactide) toughened with poly (ethylene oxide)-block-poly (butylene oxide) diblock copolymers. Macromolecules 53, 10163–10178.

Mirkhalaf, S., Fagerström, M., 2021. The mechanical behavior of polylactic acid (pla) films: fabrication, experiments and modelling. Mechanics of Time-Dependent Materials 25, 119–131.

Mises, R.v., 1913. Mechanik der festen körper im plastisch-deformablen zustand. Nachrichten von der Gesellschaft der Wissenschaften zu Göttingen, Mathematisch-Physikalische Klasse 1913, 582–592.

Mulliken, A.D., Boyce, M.C., 2006. Mechanics of the rate-dependent elastic–plastic deformation of glassy polymers from low to high strain rates. International Journal of Solids and Structures 43, 1331–1356.

Narayan, S., Anand, L., 2021. Fracture of amorphous polymers: A gradient-damage theory. Journal of the Mechanics and Physics of Solids 146, 104164.

Narisawa, I., 1972. Crazing of glassy polymers in alcohols and hydrocarbons. Journal of Polymer Science Part A-2: Polymer Physics 10, 1789–1797.

Narisawa, I., Yee, A., 2006. Crazing and Fracture of Polymers. John Wiley & Sons, Ltd.

Needleman, A., 1988. Material rate dependence and mesh sensitivity in localization problems. Computer Methods in Applied Mechanics and Engineering 67, 69–85.

Nguyen, N., Waas, A.M., 2016. Nonlinear, finite deformation, finite element analysis. Zeitschrift für angewandte Mathematik und Physik 67, 1–24.

Oxborough, R., Bowden, P., 1973. A general critical-strain criterion for crazing in amorphous glassy polymers. The Philosophical Magazine: A Journal of Theoretical Experimental and Applied Physics 28, 547–559.

Razavi, M., Cheng, S., Huang, D., Zhang, S., Wang, S.Q., 2020. Crazing and yielding in glassy polymers of high molecular weight. Polymer 197, 122445.

Reese, S., Govindjee, S., 1998. A theory of finite viscoelasticity and numerical aspects. International Journal of Solids and Structures 35, 3455–3482.

Richards, E., Rizvi, R., Chow, A., Naguib, H., 2008. Biodegradable composite foams of pla and phbv using subcritical co 2. Journal of Polymers and the Environment 16, 258–266.

Robertson, R.E., 1966. Theory for the plasticity of glassy polymers. The Journal of Chemical Physics 44, 3950–3956.

Simo, J.C., Hughes, T.J., 2006. Computational inelasticity. Springer Science & Business Media.

Simo, J.C., Oliver, J., Armero, F., 1993. An analysis of strong discontinuities induced by strain-softening in rate-independent inelastic solids. Computational Mechanics 12, 277–296.

Smith, M., 2009. ABAQUS/Standard User's Manual, Version 6.9. Dassault Systèmes Simulia Corp, United States.

Socrate, S., Boyce, M., Lazzeri, A., 2001. A micromechanical model for multiple crazing in high impact polystyrene. Mechanics of Materials 33, 155–175.

de Souza Neto, E.A., Peric, D., Owen, D.R., 2011. Computational methods for plasticity: theory and applications. John Wiley & Sons.

Sternstein, S., Ongchin, L., 1969. Yield criteria for plastic deformation of glassy high polymers in general stress fields. Polymer preprints 10, 1117–1124.

Stoclet, G., Lefebvre, J.M., Séguéla, R., Vanmansart, C., 2014. In-situ saxs study of the plastic deformation behavior of polylactide upon cold-drawing. Polymer 55, 1817–1828.

Tervoort, T., Govaert, L., 2000. Strain-hardening behavior of polycarbonate in the glassy state. Journal of Rheology 44, 1263–1277.

Tijssens, M., Van der Giessen, E., Sluys, L., 2000. Modeling of crazing using a cohesive surface methodology. Mechanics of Materials 32, 19–35.

Van Loock, F., Brassart, L., Pardoen, T., 2021. Implementation and calibration of a mesoscale model for amorphous plasticity based on shear transformation dynamics. International Journal of Plasticity 145, 103079.

Venkatesan, S., Basu, S., 2015. Investigations into crazing in glassy amorphous polymers through molecular dynamics simulations. Journal of the Mechanics and Physics of Solids 77, 123–145.

Voyiadjis, G.Z., Samadi-Dooki, A., 2016. Constitutive modeling of large inelastic deformation of amorphous polymers: Free volume and shear transformation zone dynamics. Journal of Applied Physics 119.

Wang, Z., Guo, J., Seppala, J.E., Nguyen, T.D., 2021. Extending the effective temperature model to the large strain hardening behavior of glassy polymers. Journal of the Mechanics and Physics of Solids 146, 104175.

Wu, P., Van Der Giessen, E., 1993. On improved network models for rubber elasticity and their applications to orientation hardening in glassy polymers. Journal of the Mechanics and Physics of Solids 41, 427–456.

Xiao, R., Tian, C., Xu, Y., Steinmann, P., 2022. Thermomechanical coupling in glassy polymers: An effective temperature theory. International Journal of Plasticity 156, 103361.

Yang, J., Liu, J., 2001. Cavitation of rubber particles in high-impact polystyrene. Polymer journal 33, 952–954.